PAPER • OPEN ACCESS

Overview of the results from divertor experiments with attached and detached plasmas at Wendelstein 7-X and their implications for steady-state operation

To cite this article: M. Jakubowski *et al* 2021 *Nucl. Fusion* **61** 106003

OPEN ACCESS
IOP Publishing | International Atomic Energy Agency Nuclear Fusion
Nucl. Fusion **61** (2021) 106003 (20pp) https://doi.org/10.1088/1741-4326/ac1b68

Overview of the results from divertor experiments with attached and detached plasmas at Wendelstein 7-X and their implications for steady-state operation

M. Jakubowski[1,*], M. Endler[1], Y. Feng[1], Y. Gao[1], C. Killer[1], R. König[1], M. Krychowiak[1], V. Perseo[1], F. Reimold[1], O. Schmitz[2], T.S. Pedersen[1], S. Brezinsek[3], A. Dinklage[1], P. Drewelow[1], H. Niemann[1], M. Otte[1], M. Gruca[4], K. Hammond[5], T. Kremeyer[2], M. Kubkowska[4], S. Jabłoński[4], A. Pandey[1], G. Wurden[6], D. Zhang[1], S. Bozhenkov[1], D. Böckenhoff[1], C.P. Dhard[1], J. Baldzuhn[1], D. Gradic[1], F. Effenberg[5], P. Kornejew[1], S. Lazerson[1], J. Lore[7], D. Naujoks[1], A Puig Sitjes[1], G. Schlisio[1], M. Ślęczka[8], U. Wenzel[1], V. Winters[1] and the W7-X Team[a]

[1] Max-Planck-Institut für Plasmaphysik, Greifswald, Germany
[2] University Wisconsin, Madison, United States of America
[3] Forschungszentrum Jülich, Jülich, Germany
[4] Instytut Fizyki Plazmy i Laserowej Mikrosyntezy, Warszawa, Poland
[5] Princeton Plasma Physics Laboratory, Princeton, United States of America
[6] Los Alamos National Lab, Los Alamos, United States of America
[7] Oak Ridge National Laboratory, Oak Ridge, United States of America
[8] Uniwersytet Szczeciński, Instytut Fizyki, Szczecin, Poland

E-mail: marcin.jakubowski@ipp.mpg.de

Received 31 May 2021, revised 28 July 2021
Accepted for publication 6 August 2021
Published 30 August 2021

Abstract

Wendelstein 7-X (W7-X), the largest advanced stellarator, is built to demonstrate high power, high performance quasi-continuous operation. Therefore, in the recent campaign, experiments were performed to prepare for long pulse operation, addressing three critical issues: the development of stable detachment, control of the heat and particle exhaust, and the impact of leading edges on plasma performance. The heat and particle exhaust in W7-X is realized with the help of an island divertor, which utilizes large magnetic islands at the plasma boundary. This concept shows very efficient heat flux spreading and favourable scaling with input power. Experiments performed to overload leading edges showed that the island divertor yields good impurity screening. A highlight of the recent campaign was a robust detachment scenario, which allowed reducing power loads even by a factor of ten. At the same time, neutral pressures at the pumping gap entrance yielded the particle removal rate close to the values required for stable density control in steady-state operation.

* Authors to whom any correspondence should be addressed.
[a] See Klinger *et al* 2019 (https://doi.org/10.1088/1741-4326/ab03a7) for the W7-X Team.

Keywords: divertor, stellarator, detachment, attached plasmas, power exhaust, steady-state, particle exhaust

(Some figures may appear in colour only in the online journal)

1. Introduction

Creating an interface between a high-performance fusion plasma and material surfaces is crucial in fusion energy research. However, plasma–material interaction is unavoidable because heat and particles have to leave the plasma in a controlled way. In tokamaks nowadays, this is achieved with the help of a poloidal divertor [1]. In stellarators and heliotrons, the poloidal divertor concept cannot be implemented due to the strongly non-axisymmetry of the helical plasmas. Instead, various concepts were proposed to constrain the plasma boundary by placing the divertor target plates in the three-dimensional equilibrium of the heliotrons or stellarators. The large helical device (LHD), for instance, introduced a helical divertor [2] and a local island divertor [3]. An island divertor [4] was proposed for the HELIAS line of stellarators [5] and was successfully demonstrated at Wendelstein 7-AS—the predecessor of Wendelstein 7-X. Independent on the topological differences among the divertor concepts, they need to provide the same basic functionality, which can be divided into four main tasks:

- Minimize heat and particle fluxes. To maximize the lifespan of plasma-facing components, both heat and particle fluxes to the divertor target need to be kept at a minimum. For steady-state plasma conditions in the future reactor, heat fluxes at 5 MW m^{-2} [6] and particle fluxes of 10^{20} m^{-2} s^{-1} [7] are foreseen. To reduce heat and particle fluxes to an acceptable level, energy and particle momentum need to a large degree be dissipated in the scrape-off layer (SOL) or in the vicinity of the '*upstream region*' (an area where most of the plasma coming from the core enters into the SOL) before reaching the region near divertor, often labelled in literature as the '*downstream plasma*' [8].
- Provide efficient particle exhaust. Efficient density control requires a certain level of the neutral compression. Neutral compression is defined as the ratio of the downstream (divertor) neutral pressure to the upstream (main chamber) values. This ratio should be as high as possible to provide high neutral pressure near the entrance to the divertor pumping domain and keep a low concentration of neutrals near the upstream region to avoid sputtering from the first wall due to charge-exchange of neutrals. In tokamaks, this is often achieved in the so-called '*high recycling regime*' [9], where charged plasma particles are adsorbed by the first wall and are re-released as atoms or molecules [10], many times over. Sufficient neutral pressure inside the divertor pumping volume allows for efficient removal of the excess working gas.
- Provide effective screening of impurities. Recycling of plasma particles is often associated with the release of first wall material, e.g. carbon, oxygen or tungsten. As impurities at the plasma boundary are often used to dissipate power, their presence at the plasma edge is usually required. However, too high of a concentration in the plasma core leads to poor performance or even pre-mature end of the plasma discharge. Thus, a good divertor concept needs to provide both a robust method to keep the impurities away from the plasma core and at the same time, if required by a device design, to allow a high enough concentration of those required for power dissipation by impurity radiation at the plasma edge.
- Remove helium ash. In a reactor with burning plasma, helium ash needs to be removed efficiently not to dilute the burning plasma. Also, efficient helium removal requires a high neutral compression ratio between upstream and downstream regions.

A successful divertor concept needs to provide all these features simultaneously and for as long as the plasma pulse is meant to last—in a stellarator reactor, this means steady-state.

In recent Wendelstein 7-X (W7-X) stellarator experiments, a set of large, magnetic islands in front of dedicated surfaces areas were used to define the plasma–material interface. This so-called '*island divertor*' geometry provides a very efficient way to exhaust heat and particles, which is crucial for steady-state operation. Going forward in 2022, all plasma-facing components will be water-cooled, enabling a pulse duration of up to 30 min with up to 10 MW of heating power. Consequently, in the recent campaign (called OP1.2), several experiments were performed to prepare for long pulse operation [11]. Pulses lasting tens of seconds were performed to address issues such as the development of stable detachment, control of heat and particle exhaust, and the influence of leading edges on plasma performance. The first part of this paper reports on results from attached plasmas: e.g. efficient power spreading in the SOL, and effects of small toroidal current on the topology of the island divertor and relative countermeasures, which help to cope with strike line wandering onto undesired locations. Moreover, results of purposely performed divertor overload experiments are discussed, which were used to study the resilience of plasma to a substantial release of impurities from the divertor surface. In the second part of this paper, the main results from detached plasmas are presented.

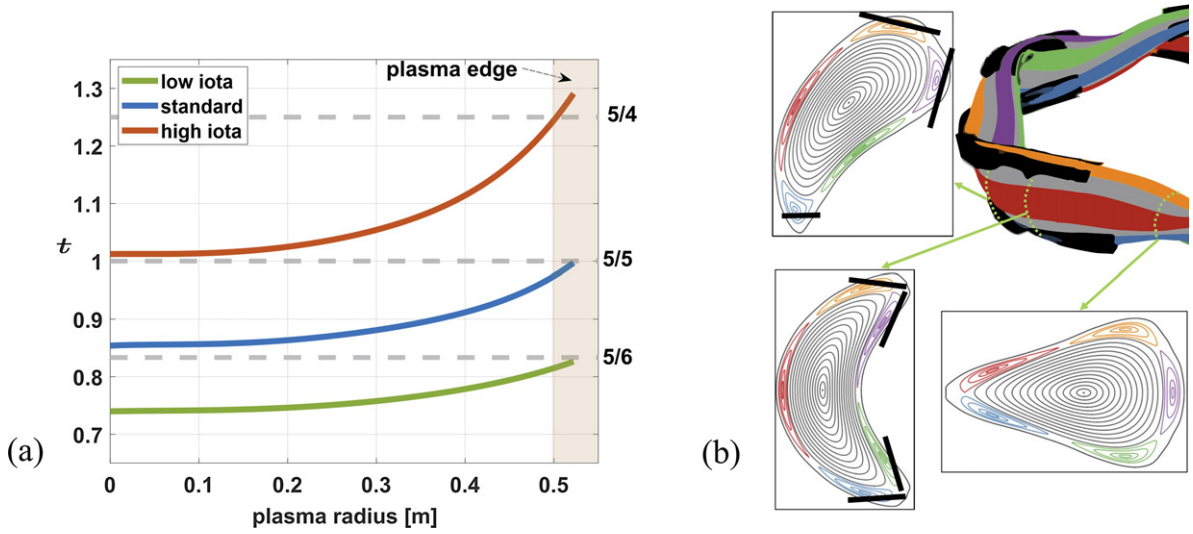

Figure 1. (*a*) Rotational transform (ι) profiles for three configurations investigated in the OP1.2 campaign. An essential aspect of these configurations from the divertor physics point of view is that they allow the formation of the exhaust channels with islands of different rotational transform and topology. (*b*) Large magnetic islands at the boundary create an interface between the plasma core and divertor target plates (marked in black). In standard configuration, 5/5 islands form 5 topologically independent SOL flux tubes.

1.1. Wendelstein 7-X

A fusion reactor based on a stellarator design has the advantage of easier access to long pulse scenarios. In fact, one of the main goals of W7-X [12] is to demonstrate high power, high performance quasi-continuous operation. W7-X has a major radius of $R \cong 5.5$ m, an aspect ratio of $A = \frac{R}{r_a} \approx 10$ (r_a is the plasma minor radius), and 5 field periods. The magnetic configuration is created by 70 modular coils: 50 non-planar and 20 planar superconducting NbTi coils [13]. The coil system comprises five non-planar and two planar (tilted) superconducting coils in each half field period.

Because coil currents in the five different types of non-planar coils and two different types of planar coils can be controlled independently, W7-X has considerable flexibility in choosing magnetic configuration [14]. Specifically, the rotational transform (ι) of magnetic field lines can be varied by 25%, as shown in figure 1. Here, the rotational transform for three main configurations investigated in the previous campaign is presented. Depending on the current distribution in the 70 superconducting coils, different island chains can appear at the plasma boundary [14]. For low-iota configuration the island chain is the $n/m = 5/6$, for standard configuration, the $n/m = 5/5$, and for high-iota, the $n/m = 5/4$. The configuration choice impacts the plasma performance in the core [15] as well as the heat and particle exhaust. The geometry of the island can be modified by the so-called control coils located behind each of the ten divertors. Additionally, to correct low-order error fields five trim coils mounted at the outer vessel are used [10].

At W7-X, ten divertor units are installed following the helical geometry of the plasma: five on top of the machine, five on the bottom. Each unit is approximately 4 m long and 1 m wide and is intersected by one or two magnetic islands. In the standard configuration (blue curve in figure 1(*a*)), five independent islands are used to create an interface between plasma core and divertor target plates, as sketched in figure 1(*b*). The islands are marked as the coloured bands in this picture.

1.2. Island divertor

The heat and particle exhaust in W7-X is realized with the help of an island divertor [4], which utilizes large magnetic islands at the plasma boundary. In the so-called 'standard configuration', $n/m = 5/5$ islands intersect ten divertor units, thus creating an interface between the plasma core (marked red in figure 1) and the divertor targets by forming the SOL (see figure 2(*a*)).

Heat and particles leave the plasma core and are directed inside the islands towards the divertor target plates. Electrons and ions lost from the confined region will circulate a few times in one or the other toroidal direction around the torus until they finally reach the target [16]. The SOL of the island divertor is to a large degree topologically equivalent to the tokamak SOL. A so-called private flux region is located in between the islands (marked with grey colour in figure 2(*a*)). Due to the three-dimensional nature of the island divertor, flux tubes of different connection length intersect the divertor target plates at different locations, resulting in the heterogeneous distribution of the power loads across the targets [17].

Areas which are not directly connected to the upstream region may receive part of the particles and energy transported from the main SOL channel [18, 19]. This situation is sketched in figure 2(*b*). The shadowed areas result from the three-dimensional shape of the island divertor and helicity of the boundary islands. The connection length of the field lines, L_c, in the shadowed regions is typically of the order of a few tens or even a few meters. In general, the physics of island divertor needs more complex transport models than in tokamaks [9], especially since cross-field transport plays an important role [20]. This results from rather small magnetic shear inside the islands, which leads to a much smaller pitch angle

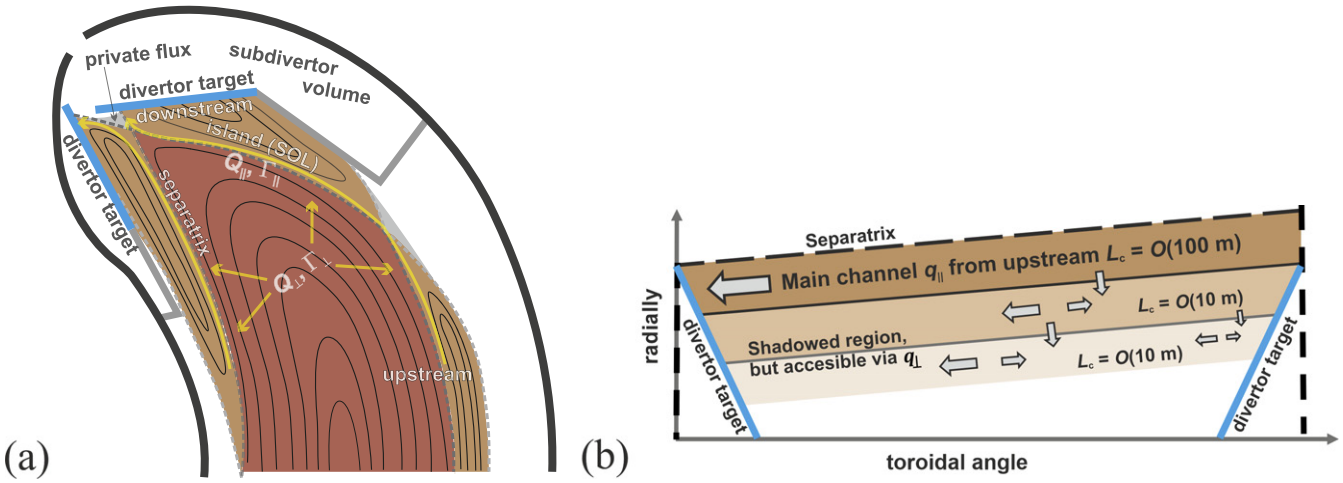

Figure 2. (*a*) Sketch of the island divertor at W7-X. Large islands at the boundary form similar to the tokamak scrape-off layer. Field lines inside the island intersect divertor target plates. The red area indicates core plasma with nested flux surfaces. (*b*) A schematic representation of transport channels in the near and far scrape-off layer of W7-X. Depending on the location of the flux tube in the scrape-off layer it will have different value of the connection length (L_c).

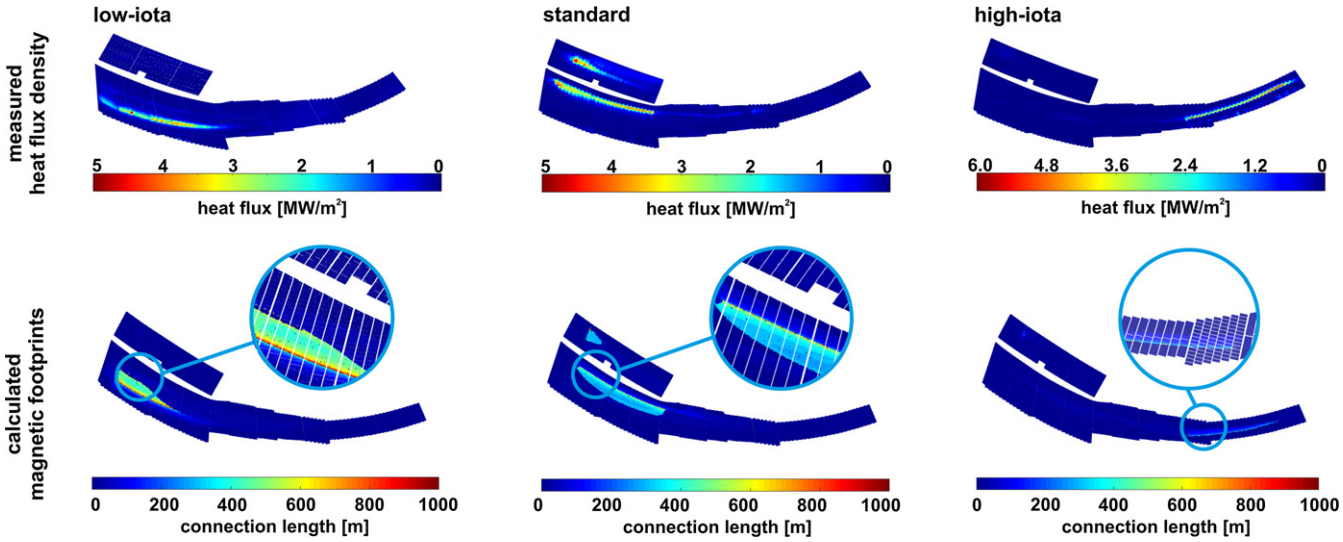

Figure 3. Strike line (top) measured by thermographic diagnostics and calculated as a distribution of connection length on the divertor surface for three configurations: left—low-iota, middle—standard and right—high-iota.

of field lines. A much smaller pitch angle in the island divertor than for a poloidal divertor in tokamaks causes perpendicular energy transport to start dominating already at temperatures of the order of a few tens eV. In contrast, in tokamaks, this effect only plays a substantial role for temperatures of about 1 eV or less, i.e. only for strongly detached plasmas [20].

2. Attached plasmas

At W7-X, ten high-resolution optical systems are used [21] to monitor the heat and particle fluxes over all ten divertor units, which allows a detailed investigation of power and particle deposition patterns. To first order, the strike line is defined by the intersection of the outermost flux surface of the edge magnetic islands with the divertor target plates. Depending on the magnetic configuration, different island chains are utilized in the island divertor, which leads to very different strike line shape on the divertor surface. The divertor at W7-X is designed to be compatible with different magnetic configurations to allow a more flexible choice of the plasma shape and properties [14]. Three examples of the so-called magnetic footprint plot [22], which show a distribution of the connection length of the field lines intersecting the divertor target plates, are shown in figure 3. For each case, the distribution of field line connection length varies with the toroidal angle, which is caused by the helical rotation of the island with increasing toroidal angle and by the shape of the divertor surface. As a result, the heat flux density distribution varies with the toroidal angle.

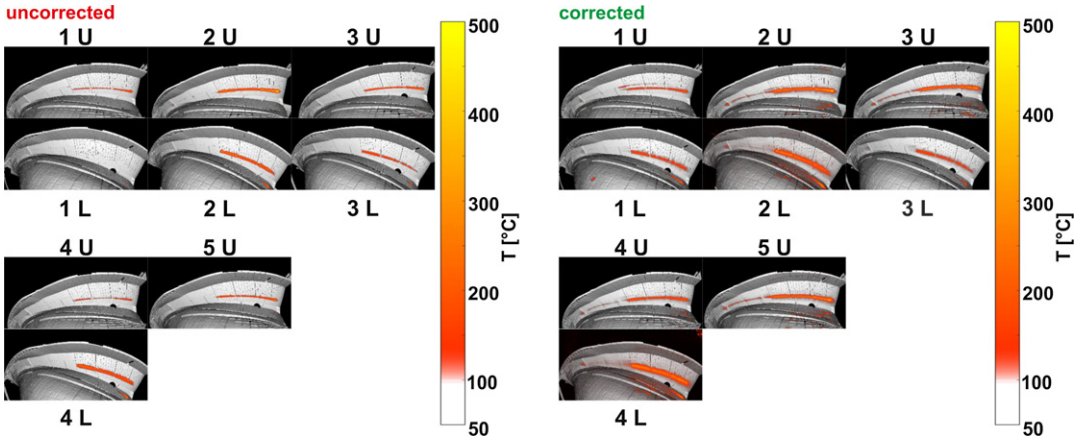

Figure 4. Surface temperatures measured at 9 out of 10 divertors in the case of standard geometry and uncorrected $n = 1$ error field (left) and minimized $n = 1$ error field (right). Number at the bottom or top of the image indicates module, U stands for upper divertor, L for lower divertor.

2.1. Error fields correction

The possible disadvantage of an island divertor is its sensitivity to external error fields and inaccuracies in the installation of plasma-facing components. The configurations, which use magnetic flux surfaces with an edge ι of 1 to form the island divertor, are particularly susceptible to the external error fields. Two types of error fields have been identified in W7-X, those which change the rotational transform and those which break the five fold symmetry of the edge island chain. Changes in ι have been measured using flux surface measurements [23] and the effect on the divertor strike lines measured [24]. Early estimates of the error fields using flux surface measurement were performed before divertor operation [25]. These results were later confirmed at full field through flux surface measurement [26]. The error fields measured are small on an absolute scale and well within the correction capabilities of W7-X. In the standard configuration two main components of the error fields with $n/m = 1/1$ and $2/2$ were estimated with the help of flux surface measurements [26]. In the first case relative strength and phase of the error field is $b_{11} = (0.55 \pm 0.25) \times 10^{-4}$, $\alpha_{11} \approx 120°$, in the latter $b_{22} = (0.6 \pm 0.2) \times 10^{-4}$, $\alpha_{22} \approx 265°$. Both components contribute to the error fields and are affecting the distribution of the power loads [27]. In figure 4, the surface temperature for 9 out of 10 divertors is shown during a discharge with uncorrected (left) and corrected b_{11} (right) error field. In the case of no-correction, a lower divertor in module 1 (1L) gets almost no heat loads, whereas divertor 4L gets on average more than others. If we define an asymmetry of the power loads by pixel-wise comparison of all ten divertors and calculated mean standard deviation, we get about 46% asymmetry for all ten divertors. Applying b_{11} correction reduces this number to 27%. The improvement is made with the help of a set of 5 trim coils energized with relatively low currents of ca 100 A [13]. A qualitative comparison of the infrared images from 9 divertors shows an equal distribution of the power loads. Nevertheless, there are remaining differences in the heat distribution, most likely from the b_{22} error field. The compensation of the b_{22} error field requires the use of so-called control coils, which are built at W7-X for strike line control. It has been successfully demonstrated for one of the magnetic configurations [18, 28]. Such compensation will be investigated during future experimental campaigns.

2.2. Effect of drifts on heat and particle fluxes

Island chains created on the $\iota = 1$ surface are most affected by the error fields coming from the imperfections of the magnetic coils and their relative position. On the other hand, 5/6 magnetic islands used in low-iota configuration were least affected by the intrinsic error fields. This feature allowed us to perform detailed studies on the edge drifts. By comparing similar plasma discharges conducted with a forward- and reverse-directed magnetic field, the impacts of drifts could be isolated through the observation of up-down asymmetries in flux profiles on the divertor targets [29]. The measurement for two discharges performed in the low-iota configuration is shown in figure 5. Depending on the magnetic field direction, either lower (for the positive direction of the magnetic field) or upper (for the negative field direction) target modules are getting more power. Also, asymmetric heat and particle fluxes were observed at the divertor surface on areas shadowed by other targets (see figure 2(*b*)) from parallel flux from the core plasma. A comparison of these asymmetric features with the magnetic footprints of magnetic field lines intersecting the divertor surface suggests that the main driver of the asymmetries at low density is poloidal $\boldsymbol{E} \times \boldsymbol{B}$ drift due to radial electric fields in the SOL and private flux regions. In higher-density plasmas, upper and lower targets collected non-ambipolar currents with opposite signs that also inverted upon field reversal. Overall, in these experiments, almost all up-down asymmetry is field-dependent and thus points to drifts as a cause.

2.3. Power flux spreading

In tokamaks, power exhaust is often characterized by the so-called 'wetted area', which is defined as power deposited to the target plates divided by the local maximum heat flux [30].

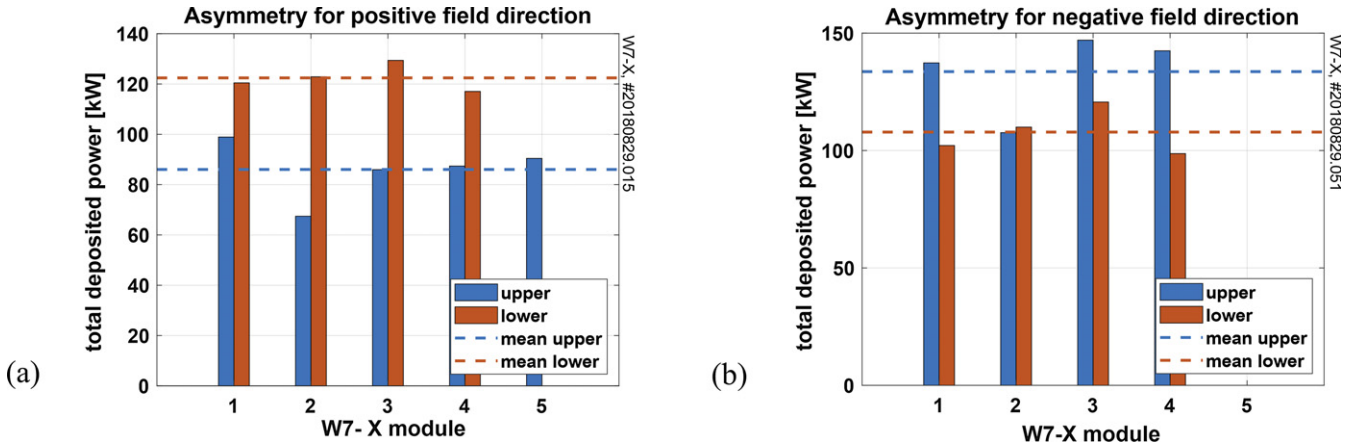

Figure 5. Distribution of divertor loads measured over nine out of ten divertor units for (*a*) positive direction of the main toroidal field and (*b*) negative direction of the toroidal magnetic field. Dashed lines indicate mean values calculated for all upper (blue) and all lower (red) divertor units.

A general definition of the wetted area is following:

$$A_{\mathrm{wet}} = \frac{P_{\mathrm{div}}}{q_{\mathrm{peak}}}.$$

In this equation, P_{div} is the total divertor power load, and q_{peak} is the maximum of the heat flux. Since the divertor has an engineering limit (e.g. $q_{\mathrm{peak}} \leqslant 10\ \mathrm{MW\ m^{-2}}$ for W7-X), this is a helpful definition. For example, for the foreseen long-pulse operation at W7-X heating power at the level of 10 MW with only 20% being radiated away, the heat flux will be within the divertor capabilities as long as the wetted area A_{w} exceeds 0.8 $\mathrm{m^2}$. Calculating this for island divertor is not as straightforward as for tokamaks [31], as heat flux distribution is strongly three-dimensional. Nevertheless, thanks to ten infrared systems [21] observing all ten divertor units, it was possible. It has been measured [32] in the OP1.2 campaign that the wetted area for plasmas run in standard configuration reached up to 1.5 $\mathrm{m^2}$—a value comparable to the much larger JET tokamak.

Moreover, as shown in figure 5, A_{wet} increases with increasing power entering the SOL. This is a promising result considering that in the subsequent campaigns, W7-X plans to increase input power and duration of its experimental programs.

The wetted area is inevitably connected to the heat transport in the SOL, as the heat and particles arrive near the divertor target along the field lines in the SOL. The most common parameter characterizing the SOL is its width λ_q [30], and it is mainly determined by competition between parallel and perpendicular transport. In tokamaks a rather narrow heat exhaust channel at the plasma edge has been observed [33]. It results in part from its geometry, namely short connection length $L_{\mathrm{c}} \sim O(10)$ (m) along the magnetic field lines between intersecting material surfaces.

In W7-X, depending on the magnetic configuration, λ_q may not particularly well describe the physics of the edge transport, especially in those configurations, where the islands are large

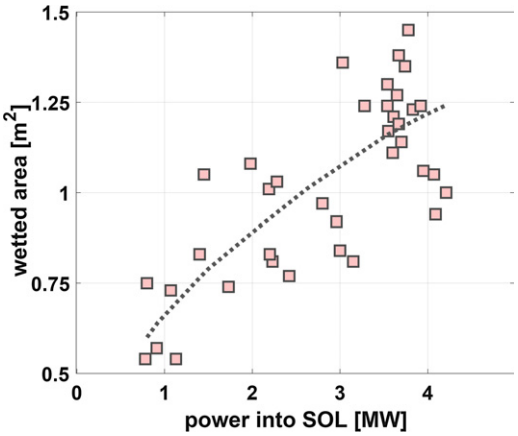

Figure 6. A wetted area as a function of power entering into the scrape-off layer for programs performed in standard configuration [19].

enough to modify the plasma edge parameters, e.g. as in the case of standard configuration [34]. For example, in standard configuration, as presented in figure 6, the magnetic island significantly influence plasma profiles in the SOL as measured by the reciprocating probe [34]. In these discharges operated at two different line integrated densities, the plasma was heated with 4.5 MW of ECRH. A Poincaré plot shows magnetic topology at the plasma cross-section, where the probe head with 22 pins was inserted into the plasma along the trajectory marked with red colour (see figure 7). Langmuir probes measured the electron temperature and electron density inside and outside the magnetic island. From both quantities, parallel heat flux is estimated according to the equation

$$q_{\parallel} = n_{\mathrm{e}} c_{\mathrm{s}} T_{\mathrm{e}},$$

where n_{e} and T_{e} are the electron density and temperature, and c_{s} denotes ion sound speed. Although this approach cannot be used for quantitative analysis as it may not reflect the width

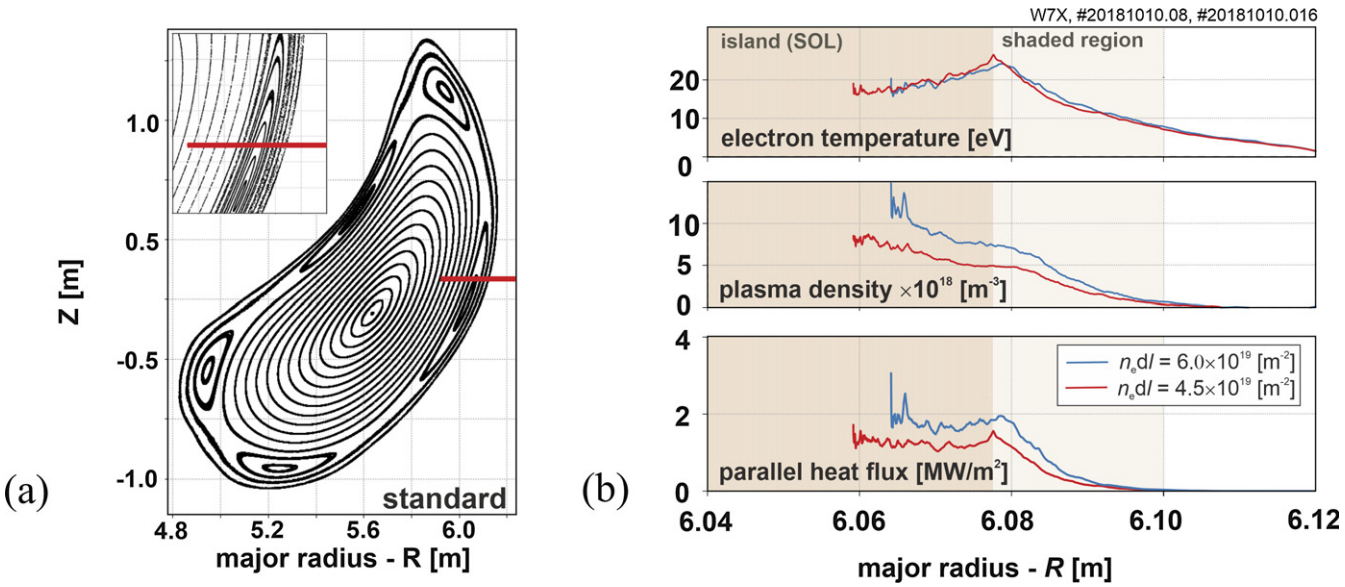

Figure 7. (*a*) Poincaré plot for the standard configuration and the longest possible path of the reciprocating probe used to measure plasma parameters. The penetration depth of the probe depends on experimental scenario and plasma parameters. (*b*) Plasma profiles measured in the scrape-off layer [34] by the reciprocating probe during two standard discharges with the same heating power of 4.5 MW and two different line integrated densities.

Table 1. Wetted area and fall-off length (*—outside of the 5/5 islands, **—incl. the 5/5 island chain) in the scrape-off layer of Wendelstein 7-X plasmas measured for the three magnetic configurations discussed in this work. Additionally, information about the connection length of field lines in the SOL is indicated; two values are provided: mean connection length calculated from all the field lines in the scrape-off layer and maximum connection length.

Configuration	Mean (max) connection length (m) [35]	Wetted area (m^2) [17, 32]	Fall off length in SOL (mm) [34]
Low-iota	320(938)	$\leqslant$1.6	10–14 4–9*
Standard	283(635)	$\leqslant$1.5	>20**
High-iota	149(418)	$\leqslant$0.5	8

of the heat flux profile on the target, it may be used to look at the fall-off length (λ_q) in the SOL. The SOL in the standard configuration—as shown in figure 7—is characterized by flat electron temperature and shallow plasma density profiles across wide magnetic islands, which makes an interpretation of λ_q calculated including the magnetic island included rather challenging. A more typical fall-off length known from limiter plasmas [18] has been measured outside the island.

The wetted area and the fall-off length are related, as both are influenced by the transport in the SOL.

Table 1 summarizes the observation for three plasma configurations: high-iota, standard and low-iota. In general, the longer the connection length of the field lines, the larger the wetted area, and the broader the SOL width. Moreover, magnetic islands significantly alter the transport at the very plasma edge, such that fall-off length (λ_q) does not fully represent the plasma behaviour there.

2.4. Overload experiments

W7-X plasma-facing components in the previous campaigns were made predominantly from graphite, making them prone to erosion due to plasma–wall interactions. Almost 50 g of carbon has been accounted for after the first half of the last campaign with a total plasma duration of nearly 3800 s [36]. During the second half of the campaign boronization of the first wall widened the operational window [37, 38]. The net erosion was significantly reduced, and only 20 g of carbon has been accounted for after the second half of the campaign, which would convert to 7.6 g of carbon per 30 min discharge [39]. Such a rate of material migration due to erosion and re-deposition raised concerns that too many impurities in the plasma core could be detrimental for long-pulse plasmas. For instance, Tore Supra carbon flakes formed on the plasma surface components, triggering events which terminated plasma discharges [40]. Therefore, an experimental session was

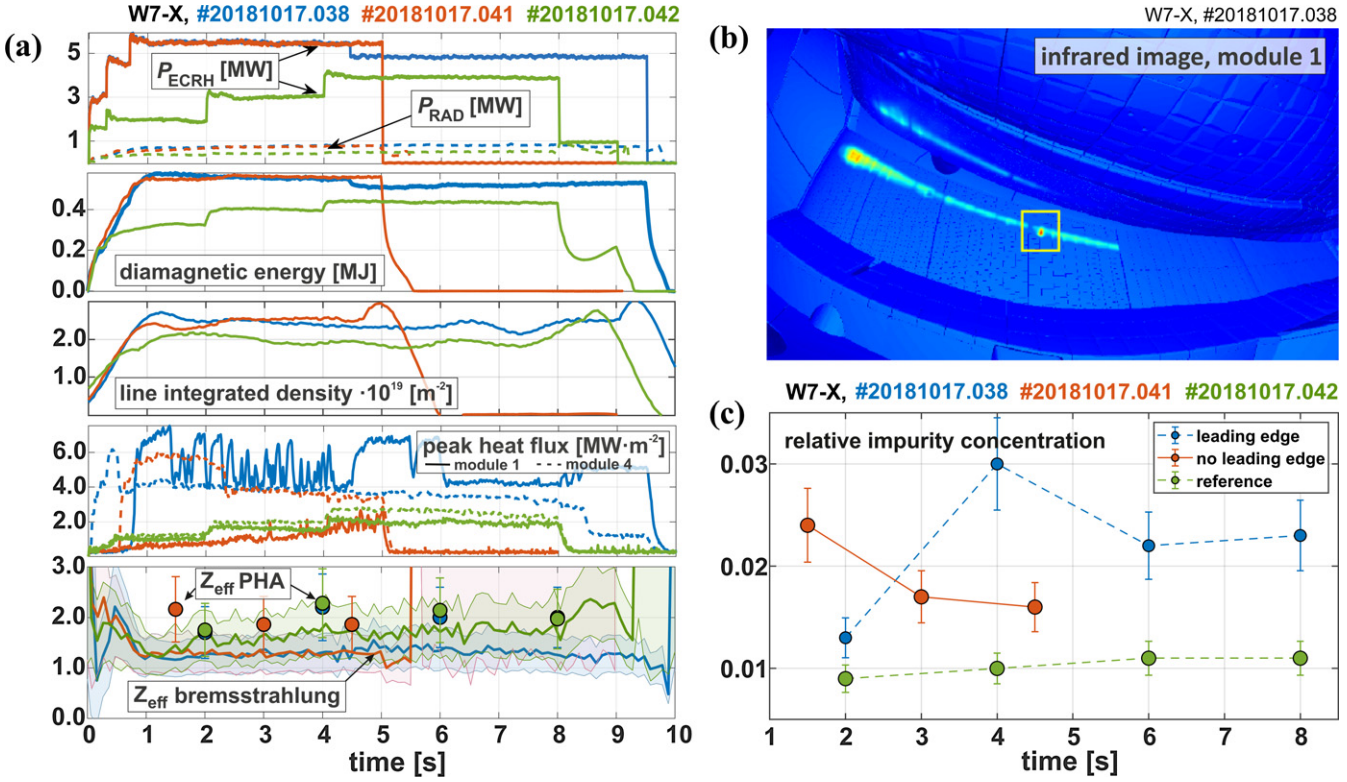

Figure 8. (*a*) Time traces for three discharges: blue—overloaded divertor (M1) with leading edge of with height of ca 0.4 mm, orange—overloaded divertor (M4) without significant leading edge, green—a reference discharge. Time traces of (from top) heating power (–) and total radiated power (–), diamagnetic energy, line integrated density, peak heat loads to divertor M1 (–) and M4 (–). Bottom panel shows Z_{eff} measured from bremsstrahlung and pulse-height analysis. (*b*) Infrared image of the divertor M1 with leading edge marked by a yellow box. (*c*) Relative concentration of impurities for chosen interval times during investigated discharges (measured by pulse height analysis).

performed to see if significant carbon emissions into the plasma would result in radiation collapses. These experiments were carried out in a quite controlled manner thanks to the flexibility of the plasma shape at W7-X. Namely, it was possible to overload a given divertor by modifying the plasma shape with the help of the external trim coils. Two divertor units were chosen for these experiments: the lower one in module 1 (labelled M1) and the lower divertor in module 4 (labelled M4). The divertor M1, overloaded during program #20181017.038, had a leading edge at the strike line with a height of ca 0.4 mm (as shown in the infrared image in figure 8(*b*)). In comparison, the divertor in module 4 (M4) without a significant leading edge was overloaded during program #20181017.041. An overview of the relevant time traces is given in figure 8(*a*). Additionally, it includes data for a W7-X reference program (#20181017.042), which was executed immediately after these experiments. All discharges survived as pre-programmed, i.e. we did not observe any early plasma termination. Both overload scenarios used 5.5 MW of heating power, of which less than 1 MW was radiated (dashed curves in the top panel of figure 8(*a*)). The fourth panel shows peak heat flux to divertor M1 (solid line) and divertor M4 (dashed line). Peak heat flux near the leading edge location was almost 7 MW m^{-2}, which corresponds to a parallel heat flux of ca 17 MW m^{-2} onto the leading edge. Correspondingly, the surface temperature at the leading edge rose above 2300 °C. Video diagnostic during the overload experiment observed strong intermittent material ejection into the plasma boundary. This lead to transient, localized radiation events and strong dithering of the local peak heat flux. This type of self-limiting' behaviour is well known for carbon plasma-facing components [41]. On the other hand, overloading divertor M4 yielded a peak heat flux at the level of 6 MW m^{-2} in module 4 and much smaller in module 1. The divertor in module 4 had smaller leading edges, and therefore the overload was not that significant, although the heat flux to the divertor was on a similar level. The most-loaded leading edge reached temperatures above 1300 °C. Although we saw locally enhanced radiation at this location, there was no ejection of carbon as observed in the other discharge. Here the main plasma parameters, including Z_{eff}, were the same as in the previous experiment. Remarkably, the strong impurity influx into the SOL had little effect on plasma performance, and Z_{eff} stayed at a relatively low level of ca 1.5. Pulse height analysis x-ray spectra in the reference discharge for chosen interval time shows that the relative concentration of carbon (i.e. in relation to the electron concentration) was on the level of 1% [42]. The contents of C and O impurities were determined based on the simulation of x-ray spectra and their comparison with the spectra collected by the PHA diagnostics. The concentration used in the simulations was changed until the experimental and simulated spectra were in good agreement. Without overloading a significant leading edge in the

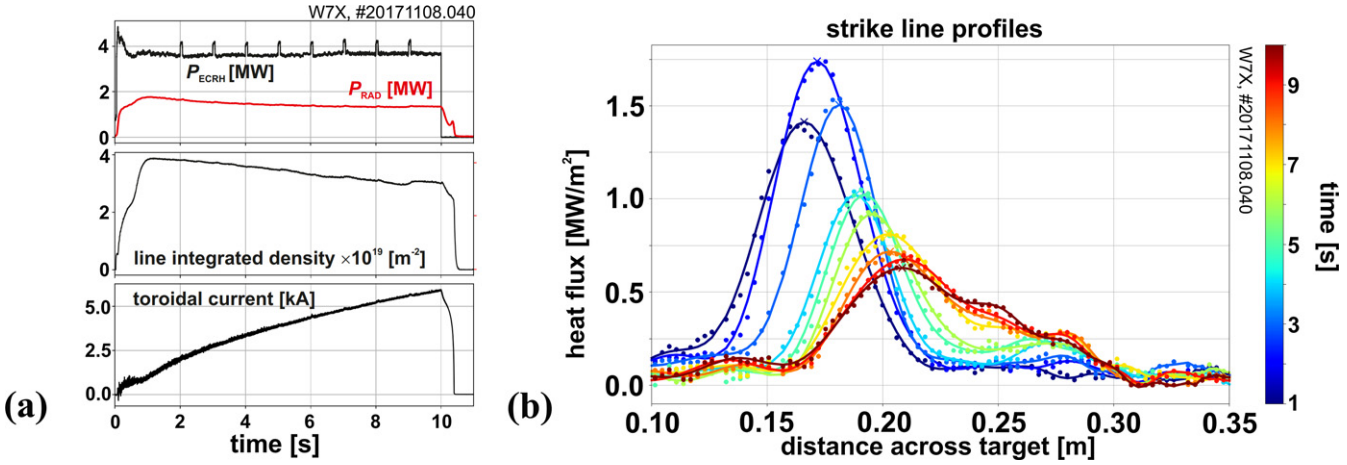

Figure 9. (*a*) Plasma parameters for discharge #20171108.040. From top: total heating (P_{ECRH}) and total radiated power (P_{RAD}), line integrated density and toroidal current. (*b*) Evolution of the strike line shown as a set of heat flux profiles across the target at different times of #20171108.040. Adapted from [46].

discharge, we started at the beginning, concentrations slightly above 2%, which then dropped below 2% throughout the program. In the discharge, with strong ejection of material into the plasma, we did not exceed 3% in the concentration of impurities, which is at a low level compared to other devices with carbon PFCs [43] and did not increase over time.

2.5. Control of the strike line position

One of the key issues addressed during the W7-X design optimization was to minimize the bootstrap currents [44]. It could not be fully realized in all magnetic configurations and plasma scenarios planned for W7-X exploitation. Residual boot strap current may be problematic as a net toroidal current modifies the edge rotational transform [45]. Due to small shear in the ι-profile (see figure 1), toroidal currents of the order of a few kA to a few tens of kA result in a radial displacement of the boundary islands. This leads to a change in the strike line position and width. An example of the strike line evolution with evolving toroidal current in the previous campaign is presented in figure 9. As discussed in [46], even small values of the toroidal current lead to significant modification of the strike line geometry. In this example, for toroidal current evolving from 0 to 2.5 kA, a shift of the strike line maximum by ∼3 cm is observed.

For higher currents, the displacement of the boundary island is large enough to influence the strike line width. At even higher values, which were not reached in this discharge, a transition from the island divertor to limiter plasmas would happen. This behaviour is linked to the effect of the plasma current on the rotational transform profile, resulting in significant inward radial shifts of the edge magnetic islands, such that they do not intersect divertor surface anymore [47]. Such an undesired scenario may be corrected by letting the plasma evolve with the increasing toroidal current, so that the desired ι-profile is reached only once Itor saturates to its final value. This is, however, connected with the movement of the strike line over the divertor surface, also across areas which are not supposed to be exposed to high values of heat flux, e.g. divertor edges near the pumping gap or even pumping gap itself. Such an overload scenario was predicted for the standard configuration with 7 MW of input power, where a steady-state toroidal current of ∼40 kA would be reached after ca 42 s [45]. Therefore, strike-line control, being one of the most critical and challenging tasks for steady-state operation, is shown to be a crucial task in a device with complex 3D magnetic topology at the plasma boundary, such as W7-X. Several measures were tested in OP1.2 to solve a challenge with component overload at the strike line location:

- An additional divertor component, the scraper element, was designed to protect the edges of the primary divertor and the pumping gap throughout this evolution during specific high-power long-pulse operational scenarios [48, 49]. It showed promising results in the discharges created to mimic the strike line geometry expected in a plasma scenario, in which the toroidal current is evolving on the *L*/*R* time ($O \sim$ few 10 s) scales from 0 kA to 43 kA. Experiments in these configurations with and without scraper-elements in different divertor modules showed that it was possible to protect the areas at the pumping gap from the overload by the strike line.
- A feed-forward or predictive control with the co- or counter electron cyclotron current drive (ECCD) [47] was applied to keep the toroidal current and its profile in the acceptable range. A certain level of the current was induced in the plasma to keep the net toroidal current close to null. By that, the edge ι stays almost constant, and the strike line does not change its position [46]. Alternatively, ECCD can help to reach a saturated value of the bootstrap current after a much shorter time than expected from the *L*/*R* time scale.
- W7-X is equipped with ten 3D-shaped control coils, which, by creating additional magnetic fields, can modulate the position and geometry of the islands and, as a result, the position of the strike line [16]. This extra field can also correct the symmetry of the field and sweep the strike line on the target in AC operation mode to avoid

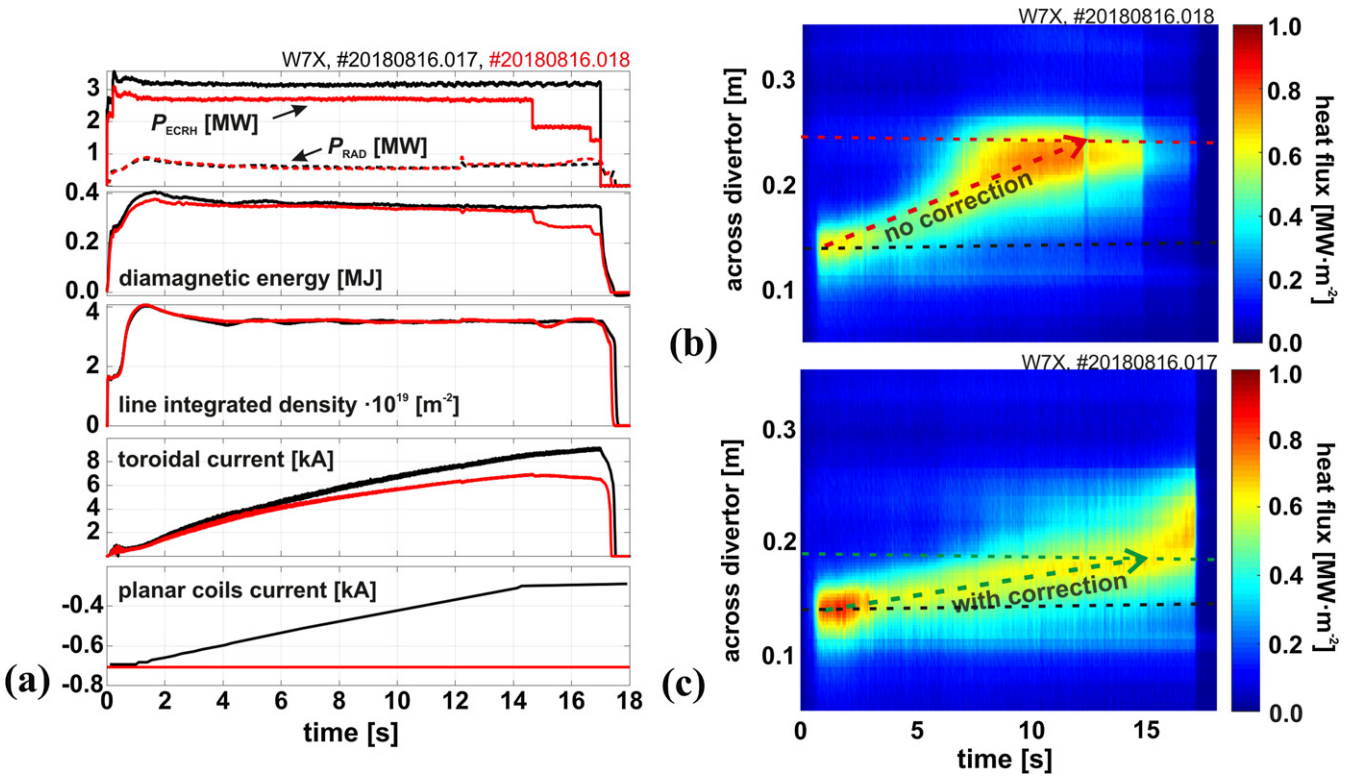

Figure 10. (*a*) Main plasma parameters for the discharge #20180816.017. From top: total heating and radiated power, diamagnetic energy, line integrated density, toroidal current and current in the planar coils. (*b*) and (*c*) Movement of the strike line due to evolving toroidal current shown as the normalized heat flux density across the strike line without edge ι correction (*b*) and with ι correction through planar coils (*c*).

local overheating or change the X-point position to control detachment. This allowed for the movement of the strike line over a few centimetres.

- Moreover, edge rotational transform can be corrected by adjusting the currents in planar and non-planar coils dynamically. A proof-of-principle experiment is shown in figure 10. In a typical standard configuration discharge during the previous campaign, both planar coils were operated with constant currents I_A, $I_B = -700$ kA, which would optimally position the island against the divertor target plates with the toroidal current close to null. As discussed earlier, the evolving toroidal current would change the edge rotational transform and, by that the strike line position. To counter-react to such a shift, the planar coils current was pre-programmed to increase steadily from -0.7 kA at $t = 1$ s to approx. -0.3 kA at $t = 15$ s. Such a change decreases edge rotational transform. In the reference discharge (#20180816.018), the planar coils current was kept constant at a value of -0.7 kA. As shown in figure 9 adjusting the planar coils current during the discharge slowed down the movement, even though the toroidal current evolved to a higher value than the reference discharge.
- Numerical studies [50] in the framework of neoclassical theory showed that by using the dependence of the bootstrap current on the plasma profile shapes, it is possible to keep the bootstrap current constant over a wide range of density and heating power. It seems to be possible as long as both quantities are varied in a coordinated way. In this case, the goal is to reach the predetermined toroidal net current at low heating power, where no overload will occur in the transient phase. Such scenarios still need to be tested experimentally during the following campaigns.

Appropriate plasma control schemes need to be qualified to ensure safe and reliable device operation, and at the same time to maximize the plasma performance. This motivation serves as a background for several studies to allow more sophisticated control mechanisms, e.g. theory-based models for plasma operation control [51]. Additionally, efforts are made to use artificial intelligence based on the actuators discussed above to control the strike line position automatically. In the case of unwanted evolution of the divertor loads or insufficient neutral pressure required for the steady-state density control, the correction would be made automatically [52].

3. Detached plasmas

Detachment features a significant reduction of incoming heat and particle fluxes across the whole divertor area, which results in reduced sputtering from the divertor surface. Higher plasma density near the divertor targets will allow higher neutral pressure in the sub-divertor volume and better neutral compression, adequate for density control and helium exhaust [53–56]. Transition into detachment results from an interplay of various

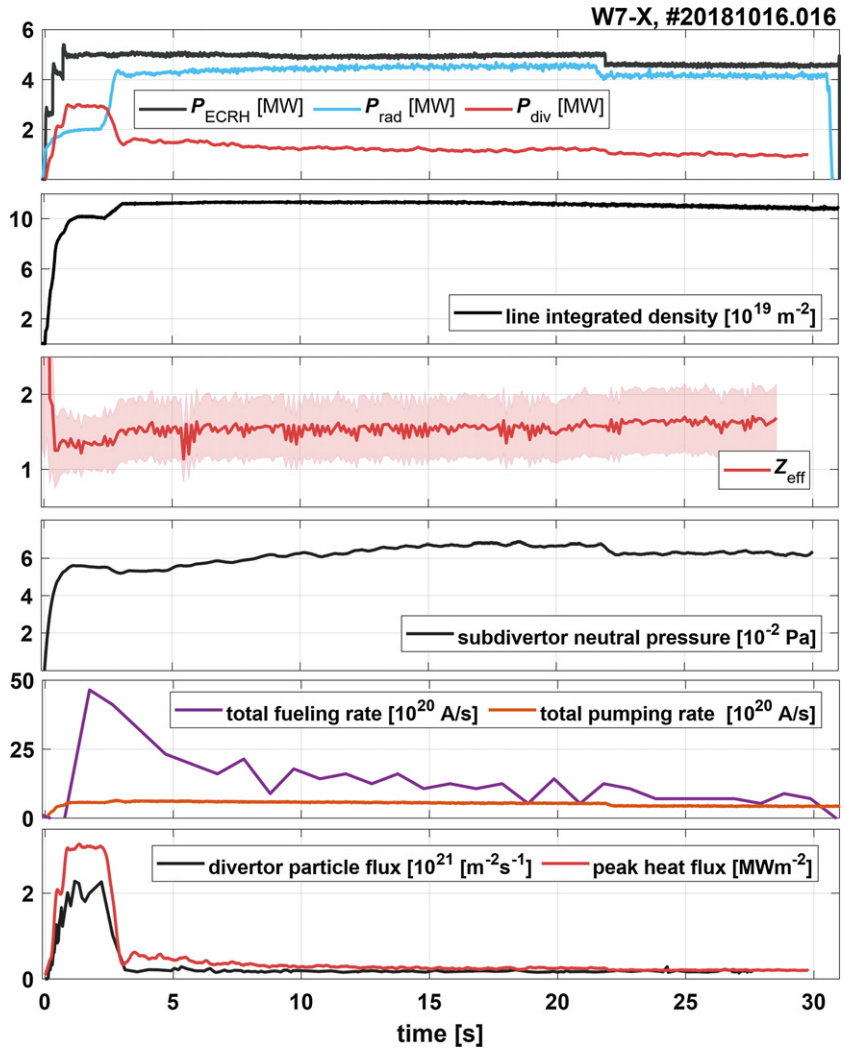

Figure 11. Time traces of the discharge with detached phase from $t \geqslant 3$s. From top to bottom: ECR heating power (P_{ECRH}), total divertor loads (P_{div}) and total radiated power (P_{rad}); line integrated density and central electron density; neutral pressure at the entrance to the pumping gap; total fueling and pumping rate and peak heat and particle fluxes to the divertor.

non-linear physics processes governing interaction between the neutral particles released from the material surfaces and steep density and temperature gradients in the plasma in front of the surface [57]. There are three important processes, which need to happen in the SOL to reach detachment: power losses, e.g. due to impurity radiation, momentum loss, e.g. due to plasma viscosity, transport and plasma–neutral interaction, and reduced particle fluxes reaching the target plates. Both tokamaks and stellarators have achieved detachment to a certain degree. Still, it was up to now more challenging in helical devices to achieve full, stable detachment due to the more complex geometry of the divertor concepts. Power detachment experiments at LHD were achieved with an increased amount of low-Z impurities at the plasma boundary, either via increased density with carbon released from the plasma-facing components or by additional seeding of nitrogen or neon. This allowed radiating away up to 40% of total input power with asymmetric reduction of the divertor power loads [58]. LHD requires additional magnetic perturbation provided by the external coils to stabilise detachment; otherwise, a strong radiation region penetrates inside the separatrix, and the plasma discharge ends in radiation collapse. At Wendelstein 7-AS, partial detachment during the so-called high density H-mode (HDH) discharges [59] was achieved. It was characterized by a partial reduction of the heat flux observed on the divertor targets and strong up-down asymmetry (up to a factor of 5) due to pronounced edge drifts.

3.1. Full thermal and stable detachment

Wendelstein 7-X demonstrated in the previous campaign relatively easy and reliable access to a stable, thermally fully detached island divertor regime [60]. This regime was realized through increasing the plasma density, in which the plasma radiation fraction f_{rad} can exceed 0.8. The main impurity during the experiments after wall-boronization at W7-X [61] was carbon, intrinsically produced by surface material erosion in the divertor. The amount of power density radiated from the carbon is given by $c_{\mathrm{c}} \times n_{\mathrm{e}}^2 \times L_z\,(n_{\mathrm{e}}, T_{\mathrm{e}})$, where c_{c} denotes the concentration of carbon impurities, n_{e}, T_{e}—the plasma electron density and temperature, and L_z is the radiated power

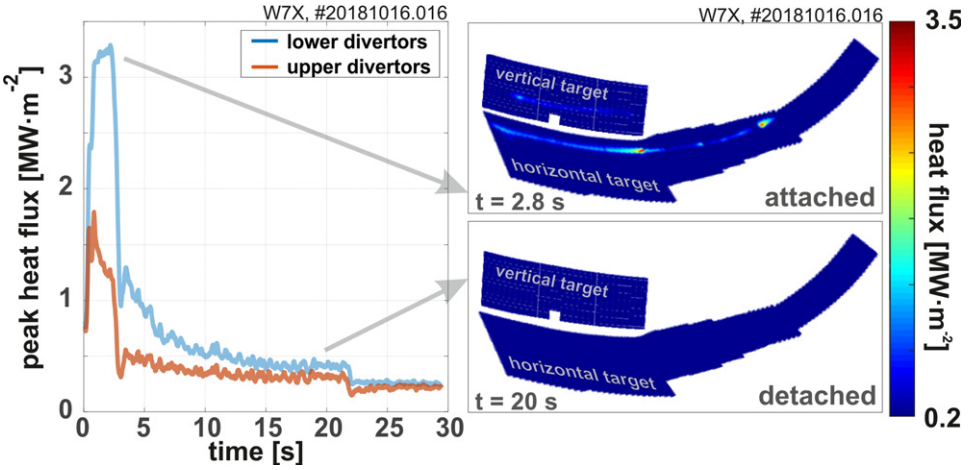

Figure 12. Evolution of heat flux during the transition to detachment. (left) Time trace of peak heat flux; (right) snapshot of averaged heat flux distribution at $t = 2$ s and $t = 20$ s.

function. Detachment provides a significant reduction of recycling flux across the whole divertor surface, while providing neutral pressure in the sub-divertor volume and neutral compression in SOL adequate for density control. In the future campaign, we will address the helium exhaust. Moreover, detachment leads to the almost complete vanishing of divertor heat fluxes over the whole divertor surface, and this plasma state can be kept stable far beyond the energy confinement time.

A detached discharge with a record duration of almost 30 s is shown in figure 11. Increasing line integrated plasma density to the level of 1.1×10^{20} m^{-2} results in a plasma radiated power fraction at the level of $f_{\mathrm{rad}} > 0.8$. The high radiation fraction reduces the total divertor loads to values below 1 MW and peak heat flux below 0.5 MW m^{-2}. This plasma state with detached power loading lasted until the pre-programmed end of the discharge. During this detached state the energy confinement time ($\tau_{\mathrm{E}} = 120$ ms) stays almost constant, as well as the central electron $T_{\mathrm{e}} \approx 2$ keV and ion temperature $T_{\mathrm{i}} \approx 1.5$ keV. During the entire detached phase, the effective charge of the plasma Z_{eff} remains low at around 1.5. This means that no significant increase of impurity concentration occurs with the cooler plasma boundary. Assuming that plasma contains only hydrogen and carbon would lead to approx.. 1.8% concentration of carbon throughout the whole discharge. Towards the end of the discharge, the particle fuelling rate (purple curve) was only slightly higher than the particle exhaust rate (red), indicating that a steady-state inventory was nearly reached, and that wall-absorption was playing a minor role. It is important to note that the drop in the peak heat flux after 22 s is caused by a dropout of one of the gyrotrons producing ECRH power; nevertheless, plasma remained stable in the detached state, showing how robust this plasma state is.

A more detailed analysis of the heat flux to the divertor surface is presented in figure 12. The left graph shows time traces of peak heat flux calculated as a maximum value of heat flux measured across all upper (red curve) and all lower (blue curve) divertors. After the transition to the detachment at $t \approx 3$ s, the peak heat flux is reduced by a factor of 8. On the right-hand side, two snapshots of the heat flux distribution on the lower divertor at $t = 2.8$ s and $t = 20$ s show that complete detachment occurs. There is no location on the divertor where peak heat flux exceeds 0.4 MW m^{-2}. In fact, almost everywhere, it stays within the limit of the diagnostic measurement (i.e. below 0.15 MW m^{-2}). Note that the heat flux contains photon contributions. Although a significant local up-down asymmetry, presumably due to edge drifts [29], is observed in the attached state at $t < 3$ s, it vanishes when transitioning into detachment. As the radiation characteristics of carbon are similar to that of nitrogen, the results obtained here should, to a large extent, be valid for detachment driven by nitrogen seeding [62].

In figure 13, profiles of divertor heat and particle fluxes across the strike line are presented. The data were obtained for another detached discharge (#20180814.025). During the transition from the attached to the detached state, it is mostly heat flux transported along the separatrix and along the field lines inside the magnetic island, that is disappearing nearly completely. In the so-called private flux region (shaded with grey colour figure 2), both heat and particle fluxes remain albeit reduced. At a high level of plasma radiation $f_{\mathrm{rad}} > 0.8$, the heat flux, which has a maximum at the separatrix, reaches a relatively low value of 0.2 MW m^{-2}. The question of why the energy and particle fluxes are more reduced inside the island cannot yet be answered experimentally due to limited island diagnostics at W7-X. However, modelling results offer some insights into the physics of the process.

Numerical studies of the transition to detachment process in stellarators are routinely performed with EMC3-Eirene—Monte Carlo fluid code [59]. The simulations made for the plasmas discussed in figure 13 are shown in figure 14 [63]. In the attached state, plasma radiation (dominated after the boronization [37] by the carbon spectral lines) is localized within the magnetic island, with a radiation band extending from the strike line to the *O*-point. As the radiation fraction increases, radiation still mostly occurs in the island region, but the radiation layer shifts closer to the separatrix. Because of

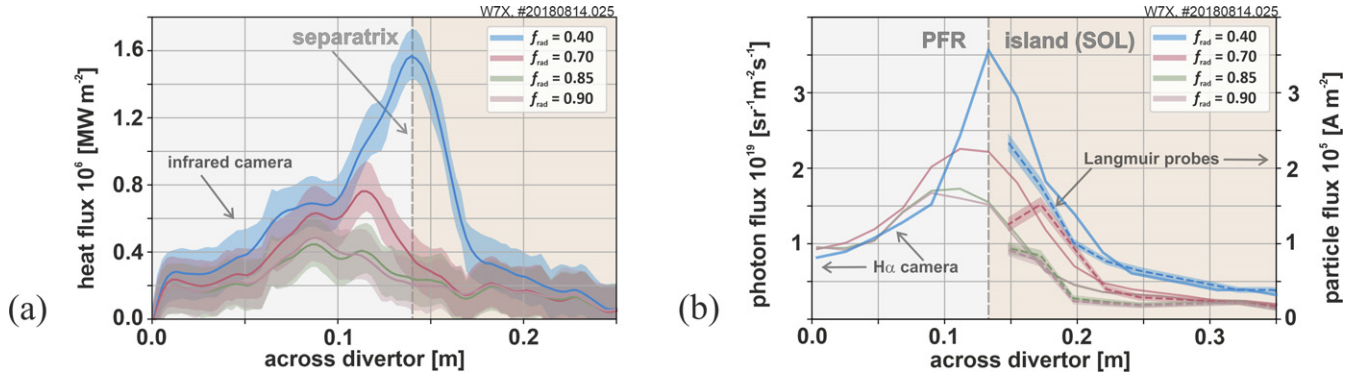

Figure 13. Profiles of heat flux (left) and particle flux (right) across the horizontal divertor target. Particle flux is measured by the Langmuir probes. Profiles are extended with the help of photon fluxes measured by a visible camera equipped with a narrow band H_α filter.

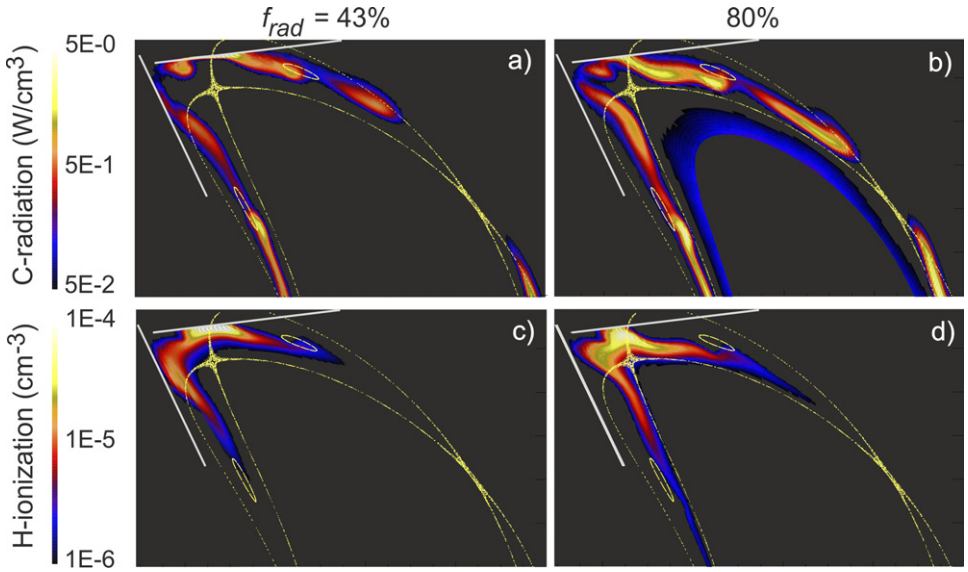

Figure 14. EMC3-Eirene modelling of carbon radiation and distribution of hydrogen ionization near the divertor target plates for discharge #20181014.025. The calculation is performed for two levels of total plasma radiation $f_{\mathrm{rad}} = 0.43$ (attached plasma) and $f_{\mathrm{rad}} = 0.80$ (detached plasma).

that, the ionization front shifts from the area at the separatrix into the private flux region. This is very well in line with changes in particle flux presented in figure 13, i.e. that during the detached phase, particle flux appears mostly in the private flux region and disappears at the target location intersected by the magnetic island.

3.2. Recycling flux and neutral pressure

Optimum divertor performance requires minimizing the divertor heat loads and maximizing sub-divertor neutral pressures and particle exhaust. With sufficient neutral pressure inside the divertor pumping volume the exhaust of main species and impurity particles can be provided while detaching the particle fluxes. This indeed happens, as shown in figure 15, where ion saturation current measured by the Langmuir probes at the divertor target as a proxy for the recycling flux is plotted

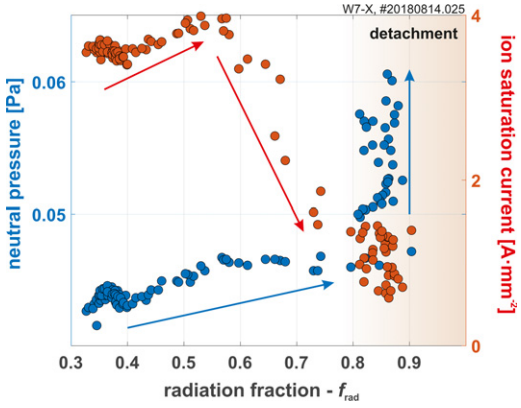

Figure 15. Neutral pressure measured at the entrance to the pumping domain of the island divertor and ion saturation current measured by the Langmuir probe at the strike line in the lower divertor of W7-X.

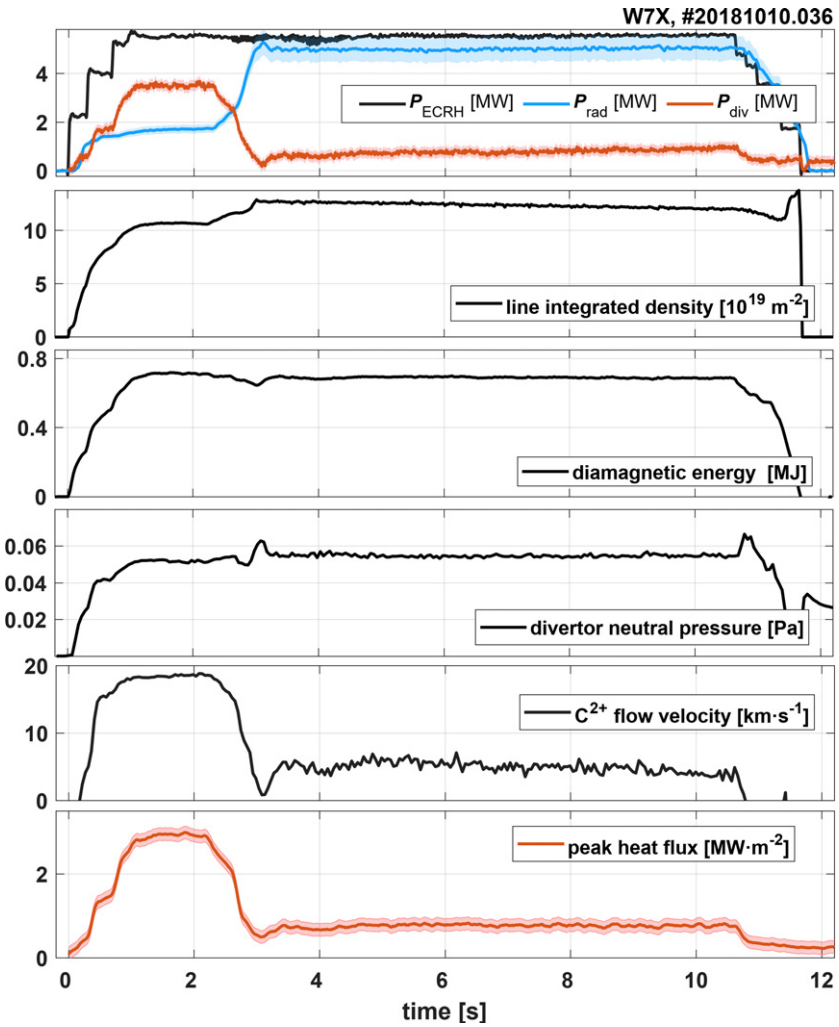

Figure 16. Time traces of the discharge with detached phase ($t \geqslant 3$ s). From top to bottom: ECRH heating power (P_{ECRH}), total divertor loads (P_{div}) and total radiated power (P_{rad}); diamagnetic energy (W_{dia}); line integrated density; peak heat flux to the divertor surface; C^{2+} flow velocity and neutral pressure at the entrance to the pumping gap.

against the radiation fraction. On the same plot, neutral pressure measured by the pressure gauge at the entrance to the subdivertor volume is shown. The highest neutral pressure behind the pumping gap is not reached at the maximum of the recycling flux (at $f_{rad} = 0.5$–0.6), but rather at f_{rad} of 80%–85%, i.e. during the detached phase. Modelling results of EMC3-Eirene [63, 64] show that two mechanisms, which happen during the detachment, are advantageous for the build-up of the neutral pressure near the entrance to the pumping domain. As the temperatures near the divertor target drop to the level of ca 5 eV [60], neutral penetration length, which is a function of plasma parameters and cross-sections for charge exchange and ionization, increases. Recent results from EMC3-Eirene for detached plasmas show [64] that the neutral penetration length near the target gets much longer compared to the attached state across the whole target. Also, CXRS processes between hydrogen ions and atoms and elastic collisions between ions and molecules lead to neutral particle trajectory changes, resulting in a higher concentration of neutrals near the pumping gap. Neutrals released from the target with very low energy have a relatively high probability of charge exchange reactions or elastic collisions with the hydrogen ions in the island region [45].

In a different but also detached discharge, it was possible to analyze plasma parameters in the downstream region, e.g. downstream density (figure 16). Here transition to detachment occurred at $t \cong 3$ s, which resulted in P_{rad} reaching more than 80% of total input power. Peak heat flux drops from 3 MW m^{-2} to ca 0.8 MW m^{-2} and stays constant until the end of the discharge. Although both heat and particle flux are strongly dropping during the transition into detachment, while neutral pressure is maintained at the same level as in the attached phase. This is enabled by a higher density in the downstream region as compared to the upstream, thanks to the high-recycling regime found in W7-X, as discussed in the following section.

3.3. Separation of counter streaming flows enables a high-recycling regime

During the previous campaign, the SOL particle parallel flow velocities were monitored with the coherence imaging

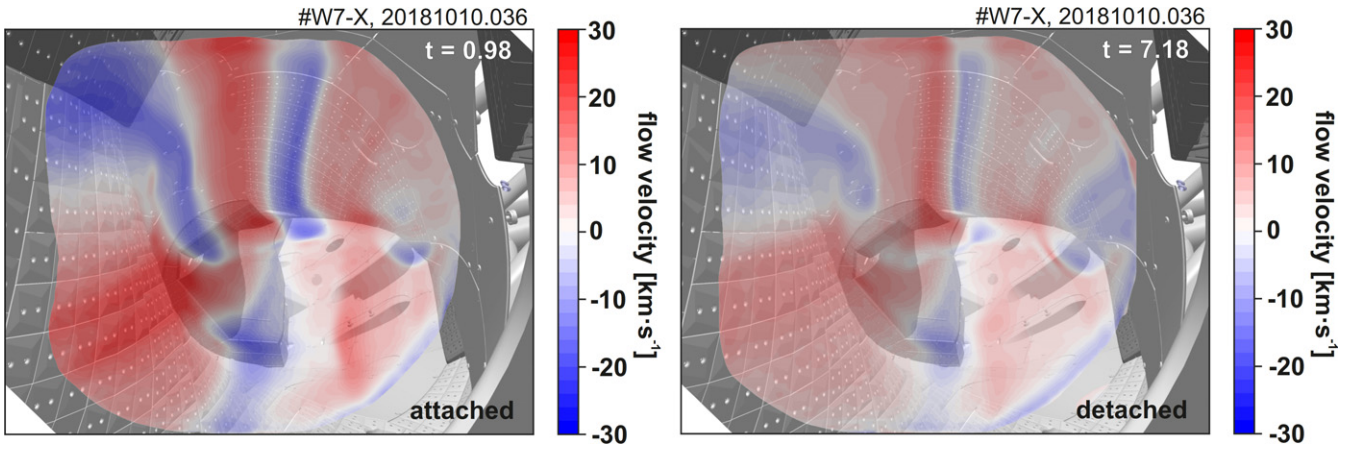

Figure 17. C^{2+} Doppler flow velocity measured by CIS [65] for the program #20181010.036, performed in the standard magnetic configuration ($I_{cc} = 1$ kA). The measurements are overlaid on a CAD model of W7-X. The displayed time point is characterized by input power $P_{ECRH} = 5.5$ MW. Positive velocities (in red) represent particle flows away from the camera, while negative ones (in blue) indicate flows towards the camera.

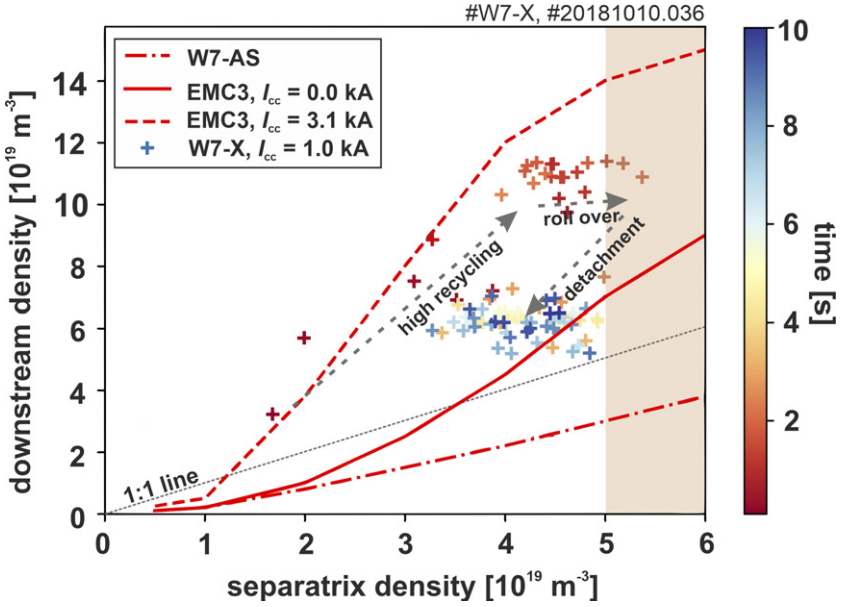

Figure 18. Divertor density evolution from Stark broadening analysis of a horizontal line of sight at the target plate shows indications of high recycling. Additionally, three curves are shown: results of predictive EMC3-Eirene modelling of the same quantities for the island geometry unmodified by the control coils ($I_{cc} = 0.0$ kA, –) and increased island width ($I_{cc} = 3.1$ kA, –). The same ratio of upstream to downstream density W7-AS [20] is shown with a dash-dotted line. Figure reproduced from [70] based on figure 12 in [20].

spectroscopy (CIS) diagnostic [65], a camera-based interferometric system capable of measuring spectroscopic quantities in 2D and deducing from that Doppler particle flows. The CIS measurements are restricted to the C^{2+} impurity passive line emission, localized in regions where $T_e \sim 10$–20 eV, i.e. close to where the hydrogen recycling atoms are ionized in the SOL. For the typical densities observed experimentally, the parallel dynamics of the C^{2+} impurity is expected to be closely coupled with the parallel flow of main plasma ions through friction, i.e. the so-called friction dominated impurity transport regime [20]. Under this assumption, the CIS results are explained with a simple 1D fluid model, in which the ionization source term plays a central role, suggesting that the ionization source is the main contributor to the particle dynamics in the region where the measurements take place [66].

During the detachment phase, the CIS diagnostic measures consistently decreased flow velocities, observed for the entire counter-streaming flow pattern typical of the magnetic island chain as visible in figure 17. This velocity drop is considered to be a consequence of the decrease in power available for ionization in the SOL [66]. A similar flow pattern has also been simulated [20] for W7-AS, where the confined plasma volume was surrounded by nine islands forming the island divertor. Wendelstein 7-AS was a much smaller device as compared to W7-X, therefore the nine islands forming the island divertor were much smaller and more closely packed at the plasma boundary [67]. As a result, counter streaming flows were not as well separated as in W7-X, and significant friction between counter-streaming ions led to strong momentum losses, preventing the high recycling regime [68].

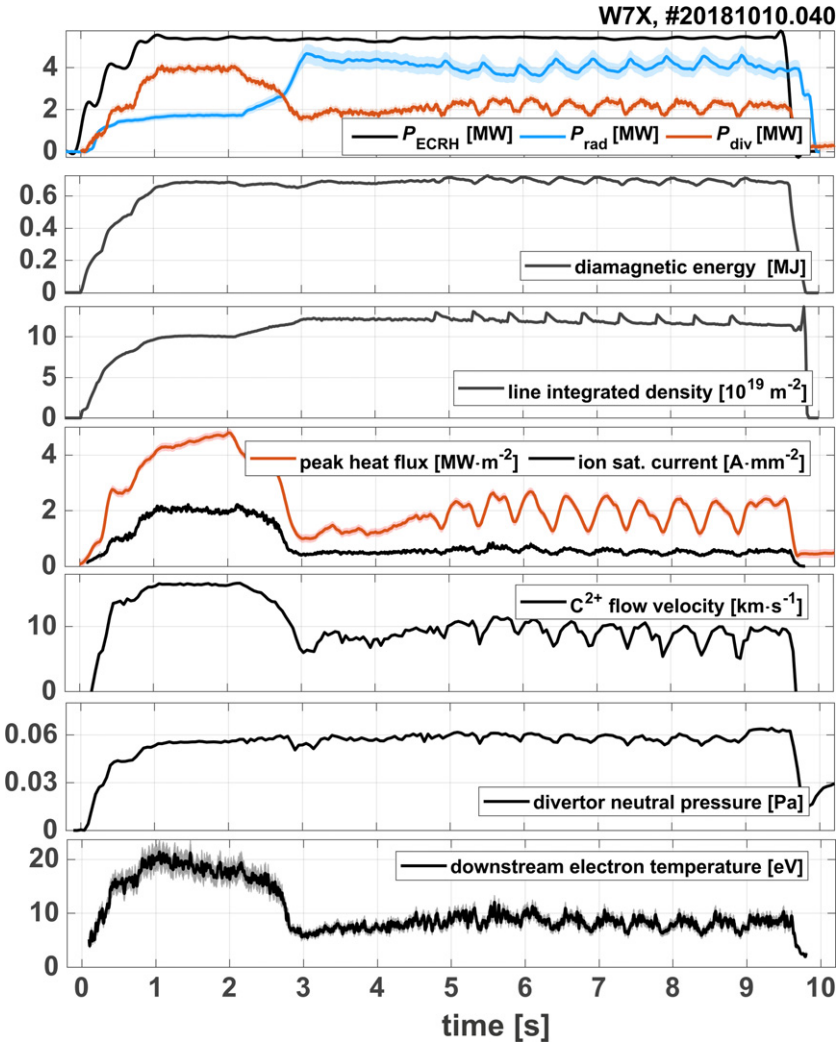

Figure 19. Time traces for W7-X #201801010.040 with 2 Hz pellet injection. From top to bottom: (1) heating power, (2) total divertor loads (P_{div}) and total radiated power (P_{rad}); diamagnetic energy (W_{dia}); line integrated density; peak heat loads and ion saturation current to Langmuir probe in lower divertor; C^{2+} flow velocity; neutral pressure at the entrance to pumping gap; electron temperature at lower divertor measured by Langmuir probe.

This is very different from the situation in the much larger device W7-X with fewer islands, where the islands and flow structures are very well separated, very similar to the situation in tokamaks. Weaker than in W7-AS momentum losses in W7-X enabled the high recycling regime.

The measurement of both quantities during program #20181010.036 is presented in figure 18. The abscissa represents plasma density measured at the separatrix by Thomson scattering [69]. The ordinate shows plasma density ca 1 cm away from the target deduced from the Stark broadening of a Balmer-line [70]. The colour of the data points indicates the time from the plasma start, as indicated by the colour bar. Before the onset of detachment, the values of the downstream electron density are significantly higher ($1.0–1.1 \times 10^{20}$ m^{-3}) than electron densities near the separatrix ($n_{e,sep}$ is in the range $4–5 \times 10^{19}$ m^{-3}). The high recycling regimes (which up to now were only observed on tokamaks) are characterized by a dense divertor plasma, which enhances the cycle of the hydrogenic particle species between the ionization in the divertor region and the neutralization on the divertor target plates before being pumped away or ionized in the confinement region. W7-AS edge plasma showed unfavourable scaling of downstream density with the upstream density, and because of that, it required very high average core plasma densities ($>2 \times 10^{20}$ m^3) to reach the upstream density of about 6×10^{19} m^{-3} required to transition into detachment [71]. Under these conditions then, however, the HDH-mode plasmas formed a very high density, recombining detached divertor plasma with high neutral pressures [71, 72]. In W7-AS, full detachment could not be achieved; all attempts to achieve that resulted in radiation collapse [73]. The magnetic flux surfaces at W7-AS were strongly compressed on the outboard side, causing a strongly localized heat loss inside the SOL, which resulted in the partially attached plasma on the target [74]. This remaining attached region was essential to screen the confined plasma from a too high influx of neutrals [59]. In contrast to W7-AS, in W7-X a localised heat outflux from the core plasma into the SOL is avoided resulting in a fairly equal radiation distribution all around the confined plasma. At W7-X, the larger

magnetic island, which can be further enlarged with the control coils, can ease the access to the high recycling regime. Such behaviour was predicted by EMC3-Eirene modelling [20] as seen from red-dashed curves, which show the predicted ratio of upstream to downstream density for the case with the small ($I_{cc} = 0$ kA) and the case with large ($I_{cc} = 3.1$ kA) magnetic island. Energizing the coils with 3.1 kA of the current increases the island width by a factor of 2 and decreases the field line connection length also by approximately a factor of 2. The geometry of the magnetic island and the distance of the strike line to the pumping gap of the divertor are important components to increase the neutral pressure [75]. The closer the strike line and hence the dominant recycling domain is located to the pump gap, the more likely it is to collect the neutrals produced by the recycling process. At separatrix density close to 5×10^{19} m^{-3} rollover and transition into detachment took place. Line ratio analysis of the Balmer lines shows that the divertor plasma in W7-X detachment conditions is ionization dominated in virtually all cases so far, and we did not observe evidence for volume recombination. More details on the high recycling regime and the plasma parameters of the downstream density at W7-X can be found in [70].

3.4. Detachment in pellet fueled discharge

As discussed above, with increasing radiation fraction, the region of highest radiation moves away from near the target to closer to the separatrix, which results in a significant drop of plasma electron temperature and thus plasma pressure at the separatrix. An important result of recent EMC3-Eirene analysis [64] shows that a reduction in recycling flux at detachment is mainly due to a drop of the plasma pressure between the LCFS and the radiation front. In a steady-state regime, W7-X will operate with continuous pellet fueling. It was rather straightforward to transition into the detachment with a sequence of pellets raising the plasma density [76]. Also an experiment was performed to see if it is possible to achieve stable detached scenarios with the plasma density stabilized with low-frequency pellet injection. An example of such a discharge is presented in figure 19, where peak heat flux is reduced from ca 5 MW m^{-2} to ca 2 MW m^{-2}, while the neutral pressure at the pumping gap is kept at 0.06 Pa. Moreover, the recycling flux (as indicated by saturation current—j_{sat}—measured by Langmuir probes in the lower divertor of module 5) is strongly reduced. As both heat and particle fluxes react in an identical way to injected pellets, it suggests that the amount of energy carried by each electron-ion pair onto targets does not vary significantly, as also shown in [64]. While recycling flux decreases (typically by more than 50%), we observe that neutral pressure at the entrance to the pumping gap is unchanged. This is important as the neutrals, which are formed either due to plasma–wall interactions or near target plasma processes, will be removed from the main chamber if they can reach the pumping gap. Due to existing leaks in the divertor closure, some of the neutrals can return to the main chamber. The neutral pressure depends on the upstream plasma parameters, which depend on the level of the plasma radiation. In the downstream region of the SOL, Langmuir probes show a

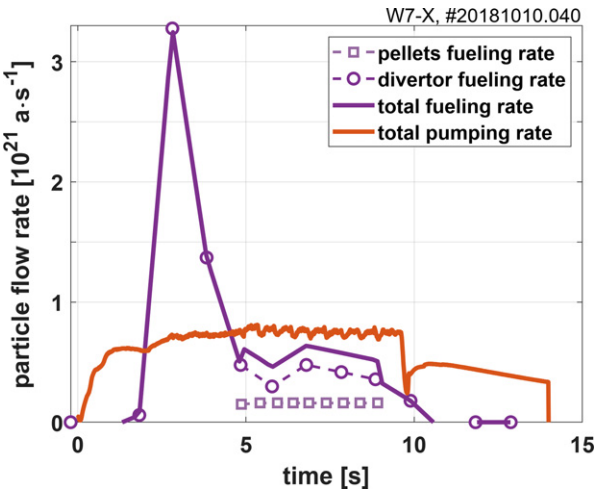

Figure 20. Particle balance for the same discharge as in figure 19. The solid purple curve shows a sum of particle flow rates from divertor gas fueling (circles) and pellet injection from LFS (squares).

drop of the electron temperature to ca 5 eV during detachment. All shown plasma downstream parameters are strongly linked to the upstream parameters and the plasma radiation. Each pellet injection (first starting at $t = 4.8$ s) leads to a transient increase of plasma radiation by ca 0.7 MW from ca 3.7 MW to ca 4.4 MW) and consequently divertor loads are reduced by the same amount. Interestingly, both divertor peak heat flux and j_{sat} measured by Langmuir probe show modulation controlled by the variation in plasma radiation.

The sensitivity of the recycling and power flux to plasma radiation can be easily understood by analysing the global power balance equation [30, 64]

$$P_{in} = \Gamma_{rec}\,(\gamma T_t + \varepsilon_i) + P_{in} \times f_{rad},$$

where P_{in} is the input power, Γ_{rec} is the recycling flux on the target plates, f_{rad}—total radiation fraction, T_t—an average target temperature, γ—the sheath transmission coefficient for ions and electrons and ε_i—the energy cost per ionization event. It has been numerically shown that T_t and ε_i at W7-X weakly depend on the radiation fraction during detachment [64]. Consequently, the resulting recycling flux and the associated power flux will be a very strong function of the radiated fraction. The flux of ions toward the divertor must drop when the plasma radiates more energy away to retain the power balance. Similar modulation with injected pellets can be observed for C^{2+} flow velocity, neutral pressure and electron temperature near the target (also measured by the Langmuir probe). It is encouraging that the neutral pressure keeps its base value of 0.06 Pa throughout the detached phase. The particle balance analysis for this discharge, cf figure 20 shows that this level of neutral pressure is not far from the level required for the steady-state density control in the next experimental campaigns. A sum of divertor fuelling rate and pellets after ca 6 s of the discharge could be reduced to the level below the total pumping rate of the turbo-molecular pumps. Depending on the pre-history of discharges, this state, which is a pre-condition for continuous plasma operation, can already be reached after a few seconds. In the next campaign, the additional sub-divertor

cryo-pumps will also be available and are expected to provide sufficient pumping capability for continuous pellet fuelling, possibly required for core density profile shaping.

4. Conclusions

A fusion reactor based on a stellarator design has the advantage of easier access to long pulse scenarios. In fact, one of the main goals of Wendelstein 7-X (W7-X), the largest optimized stellarator in the world, is to demonstrate the high performance with high power and quasi-continuous operation. Therefore, in the recent campaign, several experiments were performed to prepare for long pulse operation, addressing issues like the development of stable detachment, control of the heat and particle exhaust, and the influence of leading edges on plasma performance. The heat and particle exhaust in W7-X is realized with the help of an island divertor, which utilizes large magnetic islands at the plasma boundary. This concept shows very efficient heat flux spreading and favourable scaling with input power. Although the edge drifts introduce an asymmetry between lower and upper divertors, the peak heat fluxes during attached discharges in standard configuration, when extrapolated to 10–12 MW of input power, stay within the limits of 10 MW m^{-2} for the high heat flux divertor.

As W7-X is a low shear device, the radial position of the edge islands is sensitive to changes in toroidal current [2]. Several measures to counteract strike-line movements induced by the plasma current evolution were tested, e.g. by using external coils or ECCD. An essential issue of long pulse operation is impurity control. A series of experiments were performed to study the behaviour of intrinsic impurities and to seed low and highly recycling species to enhance plasma radiation [62]. Overall, W7-X shows good impurity control in low and high-density discharges with $T_e/T_i > 1$ when heated by ECRH alone. We have found that despite a high influx of carbon into the SOL during discharges with dedicated overloading of the leading edges, the plasmas remained stable. Line-of-sight averaged Z_{eff} stayed below 1.5 throughout the discharge, and radiation increased at the plasma edge only.

A highlight of the recent campaign was a robust detachment scenario, which allowed reducing the peak heat flux by up to a factor of 8–10. The target loads were homogeneously removed by impurity radiation and a significant reduction of the particle flux onto the target. Conditions for volume recombination of hydrogen were not reached in the divertor. At the same time, neutral pressures at the pumping gap entrance yielded a particle removal rate sufficient for stable density control over 30 s. Before the onset of detachment, the values of the downstream electron densities are significantly higher ($1.2–1.4 \times 10^{20}$ m^{-3}) than electron densities near the separatrix ($n_{e,sep}$ is in the range $4–6 \times 10^{19}$ m^{-3}). This difference between upstream and downstream density indicates that the divertor can be operated in a higher recycling regime during the attached phase. The detachment regime is characterized by low impurity concentration ($Z_{eff} = 1.5$) and sufficient neutral pressure ($p_n \leqslant 0.1$ Pa) in the sub-divertor volume for later pumping with cryo-pumps. Estimates of total exhaust rates for detached discharges at ca $0.6–0.7 \times 10^{21}$ (atoms/s) show that particle exhaust is at the level required for steady-state operation at these neutral pressures. As the radiation characteristics of carbon are similar to that of nitrogen, the results obtained here should, to a large extent, be valid for detachment driven by nitrogen seeding, as first experiments indicated [62].

The results presented in this work form a promising outlook on the overall steady-state compatibility of the detached island divertor concept in future experiments and a stellarator-based reactor.

Acknowledgments

This work has been carried out within the framework of the EUROfusion Consortium and has received funding from the Euratom research and training programme 2014–2018 and 2019–2020 under Grant Agreement No. 633053. The views and opinions expressed herein do not necessarily reflect those of the European Commission. This scientific paper has been published as part of the international project called 'PMW', co-financed by the Polish Ministry of Science and Higher Education within the framework of the scientific financial resources for 2020 under the Contract No. 5118/H2020/EURATOM/2020/2. This work was supported by the US Department of Energy (DoE) under Grants No. DE-AC02-09CH11466 and DE-SC014210.

ORCID iDs

M. Jakubowski https://orcid.org/0000-0002-6557-3497
M. Endler https://orcid.org/0000-0003-2314-8393
Y. Gao https://orcid.org/0000-0001-8576-0970
C. Killer https://orcid.org/0000-0001-7747-3066
R. König https://orcid.org/0000-0002-4772-0051
V. Perseo https://orcid.org/0000-0001-8473-9002
O. Schmitz https://orcid.org/0000-0002-9580-9149
T.S. Pedersen https://orcid.org/0000-0002-9720-1276
S. Brezinsek https://orcid.org/0000-0002-7213-3326
A. Dinklage https://orcid.org/0000-0002-5815-8463
P. Drewelow https://orcid.org/0000-0003-0121-9058
H. Niemann https://orcid.org/0000-0003-0300-1060
M. Otte https://orcid.org/0000-0003-3134-7579
M. Gruca https://orcid.org/0000-0001-7443-2250
K. Hammond https://orcid.org/0000-0002-1104-4434
T. Kremeyer https://orcid.org/0000-0002-6383-944X
M. Kubkowska https://orcid.org/0000-0003-1320-7468
G. Wurden https://orcid.org/0000-0003-2991-1484
D. Zhang https://orcid.org/0000-0002-5800-4907
S. Bozhenkov https://orcid.org/0000-0003-4289-3532
D. Böckenhoff https://orcid.org/0000-0003-1033-4648
D. Gradic https://orcid.org/0000-0002-6109-9345
F. Effenberg https://orcid.org/0000-0002-4846-4598
S. Lazerson https://orcid.org/0000-0001-8002-0121
J. Lore https://orcid.org/0000-0002-9192-465X
D. Naujoks https://orcid.org/0000-0003-4265-6078
A Puig Sitjes https://orcid.org/0000-0002-4733-6068
G. Schlisio https://orcid.org/0000-0002-5430-0645
U. Wenzel https://orcid.org/0000-0002-4107-9291
V. Winters https://orcid.org/0000-0001-8108-7774

References

[1] Janeschitz G., Borrass K., Federici G., Igitkhanov Y., Kukushkin A., Pacher H.D., Pacher G.W. and Sugihara M. 1995 *J. Nucl. Mater.* **220–222** 73
[2] Masuzaki S. *et al* 2002 *Plasma Phys. Control. Fusion* **44** 795
[3] Morisaki T. *et al* 2005 *J. Nucl. Mater.* **337–339** 154
[4] Grigull P. *et al* 2001 *Plasma Phys. Control. Fusion* **43** A175
[5] Grieger G., Nührenberg J., Renner H., Sapper J. and Wobig H. 1994 *Fusion Eng. Des.* **25** 73
[6] You J.H. *et al* 2016 *Nucl. Mater. Energy* **9** 171
[7] Pitts R.A. *et al* 2019 *Nucl. Mater. Energy* **20** 100684
[8] Stangeby P.C. and Moulton D. 2020 *Nucl. Fusion* **60** 106005
[9] Wischmeier M., Kallenbach A., Chankin A.V., Coster D.P., Eich T., Herrmann A. and Müller H.W. 2007 *J. Nucl. Mater.* **363–365** 448
[10] Marmar E.S. 1978 *J. Nucl. Mater.* **76–77** 59
[11] Pedersen T.S. *et al* 2019 *Nucl. Fusion* **59** 096014
[12] Klinger T. *et al* 2017 *Plasma Phys. Control. Fusion* **59** 014018
[13] Risse K., Rummel T., Wegener L., Holzthüm R., Jaksic N., Kerl F. and Sapper J. 2003 *Fusion Eng. Des.* **66–68** 965
[14] Geiger J., Beidler C.D., Feng Y., Maaßberg H., Marushchenko N.B. and Turkin Y. 2014 *Plasma Phys. Control. Fusion* **57** 014004
[15] Dinklage A. *et al* 2018 *Nat. Phys.* **14** 855
[16] Endler M. *et al* 2021 *Fusion Eng. Des.* **167** 112381
[17] Jakubowski M. *et al* 2018 3D heat and particle fluxes in W7-X *2018 IAEA Fusion Energy Conf.* (Gandhinaga, 22–27 October 2018) (https://conferences.iaea.org/event/151/contributions/5790/)
[18] Gao Y. *et al* 2020 *Nucl. Fusion* **60** 096012
[19] Niemann H. *et al* 2020 *Nucl. Fusion* **60** 016014
[20] Feng Y., Kobayashi M., Lunt T. and Reiter D. 2011 *Plasma Phys. Control. Fusion* 024009
[21] Jakubowski M. *et al* 2018 *Rev. Sci. Instrum.* **89** 10E116
[22] Jakubowski M.W., Abdullaev S.S. and Finken K.H. 2004 *Nucl. Fusion* **44** S1
[23] Otte M. *et al* 2016 *Plasma Phys. Control. Fusion* **58** 064003
[24] Lazerson S.A. *et al* 2019 *Nucl. Fusion* **59** 126004
[25] Lazerson S.A., Otte M., Bozhenkov S., Biedermann C. and Pedersen T.S. 2016 *Nucl. Fusion* **56** 106005
[26] Bozhenkov S.A., Otte M., Biedermann C., Jakubowski M., Lazerson S.A., Sunn Pedersen T. and Wolf R.C. 2018 *Nucl. Fusion* **59** 026004
[27] Lazerson S.A. *et al* 2018 *Plasma Phys. Control. Fusion* **60** 124002
[28] Gao Y., Jakubowski M.W., Drewelow P., Pisano F., Puig Sitjes A., Niemann H., Ali A. and Cannas B. (Team W.-X.) 2019 *Nucl. Fusion* **59** 066007
[29] Hammond K.C. *et al* 2019 *Plasma Phys. Control. Fusion* **61** 125001
[30] Stangeby P.C. 2000 *The Plasma Bounday of Magnetic Fusion Devices* (*Plasma Physics Series*) (Bristol: Insitute of Physics Publishing)
[31] Jakubowski M.W. *et al* 2009 *Nucl. Fusion* **49** 095013
[32] Niemann H. *et al* 2020 *Nucl. Fusion* **60** 084003
[33] Eich T. *et al* 2013 *Nucl. Fusion* **53** 093031
[34] Killer C. *et al* 2019 *Nucl. Fusion* **59** 086013
[35] Sinha P., Hölbe H., Pedersen T.S. and Bozhenkov S. 2017 *Nucl. Fusion* **58** 016027
[36] Mayer M. *et al* 2020 *Phys. Script.* **T171** 014035
[37] Sereda S. *et al* 2020 *Nucl. Fusion* **60** 086007
[38] Fuchert G. *et al* 2020 *Nucl. Fusion* **60** 036020
[39] Brezinsek S. *et al* 2021 Plasma–surface interaction in the stellarator W7-X: conclusions drawn from operation with graphite plasma-facing components *Nucl. Fusion* (private communication)
[40] Ekedahl A. *et al* 2009 *J. Nucl. Mater.* **390–391** 806
[41] Stork D., Jones T.T.C., Clement S., Morgan P.D., Reichle R., Saibene G., Sartori R., Summers D.D.R. and Tagle J.A. 1990 *J. Nucl. Mater.* **176–177** 409
[42] Kubkowska M. *et al* 2018 *Fusion Eng. Des.* **136** 58
[43] Pugno R. *et al* 2001 *J. Nucl. Mater.* **290–293** 308
[44] Grieger G. *et al* 1992 *Phys. Fluids* B **4** 2081
[45] Geiger J., Beidler C.D., Drevlak M., Maaßberg H., Nührenberg C., Suzuki Y. and Turkin Y. 2010 *Contrib. Plasma Phys.* **50** 770
[46] Gao Y. *et al* 2019 *Nucl. Fusion* **59** 106015
[47] Killer C. *et al* 2019 *Plasma Phys. Control. Fusion* **61** 125014
[48] Lore J.D., Cianciosa M., Frerichs H., Geiger J., Hoelbe H. and Boscary J. 2018 *IEEE Trans. Plasma Sci.* **46** 1387
[49] Lore J.D. *et al* 2019 *Nucl. Fusion* **59** 066041
[50] Sinha P., Böckenhoff D., Endler M., Geiger J., Hölbe H., Smith H.M., Pedersen T.S. and Turkin Y. 2019 *Nucl. Fusion* **59** 126012
[51] Dinklage A. *et al* Theory-based models for the control of W7-X divertor plasmas *Nucl. Fusion* (private communication)
[52] Pisano F., Cannas B., Fanni A., Sias G., Gao Y., Jakubowski M., Niemann H. and Puig Sitjes A. 2020 *Plasma Phys. Control. Fusion* 025009
[53] Krasheninnikov S.I. and Kukushkin A.S. 2017 *J. Plasma Phys.* **83** 155830501
[54] Leonard A.W. 2018 *Plasma Phys. Control. Fusion* **60** 044001
[55] Loarte A. *et al* 1998 *Nucl. Fusion* **38** 331
[56] Miyazawa J. *et al* 2006 *Fusion Sci. Technol.* **50** 192
[57] Stangeby P.C. 2018 *Plasma Phys. Control. Fusion* **60** 044022
[58] Kobayashi M., Masuzaki S., Tanaka K., Tokuzawa T., Yokoyama M., Narushima Y., Yamada I., Ido T. and Seki R. 2018 *Nucl. Mater. Energy* **17** 137
[59] Feng Y. *et al* 2005 *Nucl. Fusion* **45** 89
[60] Schmitz O. *et al* 2021 *Nucl. Fusion* **61** 016026
[61] Wauters T. *et al* 2018 *Nucl. Mater. Energy* **17** 235
[62] Effenberg F. *et al* 2019 *Nucl. Fusion* **59** 106020
[63] Feng Y., Beidler C.D., Geiger J., Helander P., Hölbe H., Maassberg H., Turkin Y. and Reiter D. 2016 *Nucl. Fusion* **56** 126011
[64] Feng Y. *et al* 2021 *Nucl. Fusion* **61** 086012
[65] Perseo V., Gradic D., König R., Ford O.P., Killer C., Grulke O. and Ennis D.A. (Team W.-X.) 2020 *Rev. Sci. Instrum.* **91** 013501
[66] Perseo V. *et al* Direct 2D measurements of parallel counter-streaming flows in the W7-X scrape-off layer for attached and detached plasmas *Nucl. Fusion* (private communication)
[67] Hirsch M. *et al* 2008 *Plasma Phys. Control. Fusion* **50** 053001
[68] König R. 2021 *24th Int. Conf. Plasma Surface Interaction in Fusion Devices* (Jeju, 25–29 January 2021) (https://psi2020.kr/)
[69] Pasch E., Beurskens M.N.A., Bozhenkov S.A., Fuchert G., Knauer J. and Wolf R.C. (Team W.-X.) 2016 *Rev. Sci. Instrum.* **87** 11E729
[70] Reimold F. *et al* 2020 Experimental indications of high-recycling and the role of pressure and power dissipation for detachment at W7-X *2020 IAEA Fusion Energy Conf.* (Nice, 10–15 May 2021) (https://conferences.iaea.org/event/214/contributions/17514/)
[71] Thomsen H., König R., Feng Y., Grigull P., Klinger T., McCormick K., Ramasubramanian N. and Wenzel U. 2004 *Nucl. Fusion* **44** 820

[72] Wenzel U., König R. and Pedersen T.S. 2014 *Nucl. Fusion* **55** 013017
[73] McCormick K., Grigull P., Burhenn R., Ehmler H., Feng Y., Giannone L., Haas G. and Sardei F. 2005 *J. Nucl. Mater.* **337–339** 520
[74] Feng Y., Frerichs H., Kobayashi M. and Reiter D. 2017 *Plasma Phys. Control. Fusion* **59** 034006
[75] Sharma D., Feng Y., Sardei F., Kisslinger J., Grote H., Grigull P. and Renner H. 2005 *J. Nucl. Mater.* **337–339** 471
[76] Zhang D. *et al* 2019 *Phys. Rev. Lett.* **123** 025002